EFFECT OF CORROSION ON FATIGUE PERFORMANCE OF STEEL ROBOTIC WELDS FOR UNDERWATER MARINE COMPONENTS

ALEXANDROS G. OIKONOMOU

MSC IN WELDING ENGINEERING

A THESIS SUBMITTED IN PARTIAL FULLFILLMENT FOR THE DEGREE OF DOCTOR OF PHILOSOPHY

SUPERVISOR: PROFESSOR GEORGE A. AGGIDIS

ENGINEERING DEPARTMENT, FACULTY OF SCIENCE AND TECHNOLOGY, LANCASTER UNIVERSITY, UNITED KINGDOM

Declaration

The author declares that this thesis has not been previously submitted for award of a higher degree to this or any university, and that the contents, except where otherwise stated, are the author's own work.

Signed: Alexandros G. Oikonomou

Date: 29/11/2024

Abstract

Corrosion is a critical factor that significantly impacts the fatigue performance of welded structures subjected to marine environments. Investigations into corrosion fatigue typically involve deriving S-N curves through testing of specimens that have undergone varying degrees of corrosion. However, there is a paucity of research specifically addressing the comparative fatigue behavior of pre-corroded and non-corroded specimens. This study aims to bridge this gap by conducting systematic fatigue tests on pre-corroded specimens alongside their non-corroded counterparts. This dual approach facilitates a more comprehensive understanding of the effects of corrosion on both the initiation and propagation of fatigue cracks.

A key innovation in the current research is the use of state-of-the-art robotic welding, specifically employing the FCAW process, for specimen preparation. Robotic integration in welding processes offers several advantages, including enhanced consistency in weld quality and improved repeatability over extended durations. This method also introduces flexibility, allowing for more complex welding geometries to be achieved with precision. These benefits are particularly critical for fatigue testing, where weld consistency is paramount to ensure reliable results.

The literature review highlights a scarcity of data on the fatigue performance of HY100 steel and 316Ti stainless steel in corroded conditions, despite their extensive use in marine and demanding environments. This contrasts with the relatively well-documented fatigue behavior of S355 steel welds, which, however, have seldom been studied using robotic welding technologies. By focusing on HY100 and 316Ti weldments and employing robotic FCAW, this study fills a significant research gap and contributes new insights into the corrosion fatigue performance of these materials.

The anticipated outcomes—derived from fatigue experiments, fractographic analyses, and metallographic studies—are expected to substantially enhance the existing knowledge base. By exploring under-studied materials and methods, particularly the implications of robotic FCAW on corrosion fatigue, this research provides novel findings that can inform both academic research and industrial practices. These contributions are especially relevant given the lack of comparable data, emphasizing the importance of this study in advancing the understanding of corrosion fatigue mechanisms in marine structural applications.

Keywords

welding current; welding voltage; welding speed; HY 100 steel; heat input; FCAW; microscopic examination; corrosion resistance; weldability; marine systems; Flux Cored Arc Welding; Hydrogen Induced Cracking

Acknowledgments

I would like to thank my academic supervisor Dr. George Aggidis for his great support and continuous encouragement during this PhD research.

Peer-reviewed journal publications

1. Oikonomou, A. G., & Aggidis, G. A. (2019). Material aspects of underwater marine systems in Greece. Materials Today: Proceedings, 10(Part 3), 419–429. https://doi.org/10.1016/j.matpr.2019.03.005

2. Oikonomou, A. G., & Aggidis, G. A. (2019). Determination of optimum welding parameters for the welding execution of steels used in underwater marine systems (including the submerged parts of Wave Energy Converters). *Materials Today: Proceedings, 18*(Part 2), 455–461. https://doi.org/10.1016/j.matpr.2019.06.211

3. Oikonomou, A. G., & Aggidis, G. A. (2021). Determination of the corrosion resistance of the welded steels used in underwater marine systems (including the submerged parts of wave energy converters). *Materials Today: Proceedings, 44*(Part 7), 5048–5053. https://doi.org/10.1016/j.matpr.2020.06.393

Table of Contents

List of Figures

List of Tables

Acronyms

AWS	American Welding Society
CCT	Continuous Cooling Transformation
DOE	Design of Experiments
EGW	Electrogas Welding
FCAW	Flux-Cored Arc Welding
FCAW-G	Gas-Shielded Flux-Cored Arc Welding
FCAW-S	Self-Shielded Flux-Cored Arc Welding
HAZ	Heat-Affected Zone
HIC	Hydrogen-Induced Cracking
HY100	High-Yield Steel with 100 ksi tensile strength
IIW	International Institute of Welding
SEM	Scanning Electron Microscope
SMAW	Shielded Metal Arc Welding
W1	Initial mass before exposure
W2	Mass after exposure

Chapter 1. Introduction

The selection of suitable materials for the construction of various welded underwater marine systems is governed by critical properties such as (a) excellent mechanical properties (yield strength, tensile strength, hardness, toughness at low temperatures, ductility, weldability, fatigue performance), (b) high corrosion resistance, (c) local environmental factors (e.g. sea salinity, the velocity of seawater, temperature, depth of immersion) which affect the corrosion rate (d) high life durability and low degree of maintenance, (e) economic factors (cost of raw material, cost of maintenance, cost of installation and removal). Improving the quality and reliability of existing underwater welded systems requires a focus on two key aspects: weldability and fatigue performance under pre-corrosive environments. To address these challenges, this PhD research investigates three distinct welded materials (HY100 steel, 316Ti stainless steel, and S355J2N steel) and their contribution in the improvement of the quality and reliability of existing underwater welded systems.

Material Properties

The development of high-strength steels like HY100 (yield strength exceeding 100,000 psi or 690 N/mm^2) has been instrumental in advancing underwater structural performance to explosion shocks. Originally designed in 1962 for the U.S. Navy, HY100 features a tempered bainite and martensite microstructure, making it suitable for submarines, offshore platforms, and pressure vessels and is the basic material for the development of ultra high strength steels. However, challenges such as hydrogen-assisted cracking (HAC) during the welding process remain significant. These issues, attributed to high quality welding wires, low preheat temperatures, and rapid cooling rates, have been mitigated through optimized welding parameters, including preheating and post-weld heating (Sadiq et al., 2015).

Austenitic stainless steel 316Ti, stabilized with titanium, offers exceptional resistance to corrosion and stress corrosion cracking (SCC) in chloride-rich environments. The inclusion of titanium prevents carbide precipitation, improving mechanical performance at elevated temperatures (Alaskari et al., 2014). Surface treatments, such as grinding and shot peening, further enhance resistance to SCC by refining surface integrity and residual stress profiles (Liu & Zhang, 2024). These attributes make 316Ti an ideal choice for applications requiring high corrosion resistance and mechanical stability in harsh environments.

S355J2N, a hot-rolled structural steel, is valued for its balance of mechanical properties and cost-effectiveness, making it widely applicable in construction and marine systems. Its weldability and toughness provide an excellent foundation for studying corrosion and fatigue performance in controlled conditions.

The selection of HY100, 316Ti stainless steel, and S355J2N for this study is driven by their distinct mechanical and metallurgical characteristics, as well as their relevance to industrial applications where structural integrity, corrosion resistance, and weldability are critical. HY100 steel was chosen due to its widespread use in naval and subsea applications where high strength, fracture toughness, and resistance to extreme hydrostatic pressures are essential. Its susceptibility to hydrogen-assisted cracking during welding makes it an ideal candidate for investigating weldability challenges and developing optimized welding procedures, particularly for flux-cored arc welding (FCAW) in high-strength steel systems. In contrast, 316Ti stainless steel represents a class of corrosion-resistant alloys engineered for aggressive, chloride-rich environments. Its inclusion in this study provides an opportunity to evaluate how metallurgical stabilization through titanium additions influences welding behaviour, stress corrosion cracking susceptibility, and surface integrity under simulated service conditions. S355J2+N was selected as a baseline structural steel due to its excellent balance of strength, weldability, and availability, making it a logical reference material for comparative analysis of microstructural evolution, corrosion performance, and mechanical behaviour across different welding conditions. By incorporating materials with diverse mechanical strengths, metallurgical characteristics, and environmental performance requirements, this study enables a comprehensive evaluation of welding processes across a range of industrially relevant scenarios, while also generating insights that can be applied to the fabrication and maintenance of critical marine, offshore, and structural systems.

Flux Cored Arc Welding Process

Flux-Cored Arc Welding (FCAW) was first introduced at the AWS Exposition in Buffalo, New York, in May 1954 (American Welding Society Handbook, 1998). Developed to address industrial demands, FCAW effectively combines the strengths of Shielded Metal Arc Welding (SMAW), Gas Metal Arc Welding (GMAW), and Submerged Arc Welding (SAW) (Jeffus, 2020). This process employs a flux-cored wire instead of a solid bare wire, enhancing its versatility for joining materials like carbon and low-alloy steels, stainless steels, and cast and wrought irons. Widely adopted since 1957, FCAW has undergone continuous development,

with equipment advancements extending its application scope, including its integration into Electrogas Welding (EGW) (Minnick, 2010).

FCAW generates an electric arc between a continuously fed flux-cored electrode wire and the workpiece, creating the heat required to melt the electrode and base material. This produces a weld pool shielded from atmospheric contamination by gases and slag generated from the flux within the electrode. Depending on the electrode type, FCAW operates in two modes: self-shielded (FCAW-S), which relies solely on flux-generated shielding gases, and gas-shielded (FCAW-G), which uses external gases like CO_2 or an argon-CO_2 mix for added protection (Jeffus, 2020). FCAW's high deposition rates, deep penetration capabilities, and adaptability to various welding positions, including overhead and vertical, make it suitable for thick materials and demanding industries like shipbuilding, heavy equipment manufacturing, and offshore construction (Althouse et al., 2020). The gas shielded process is illustrated schematically in figure 1:

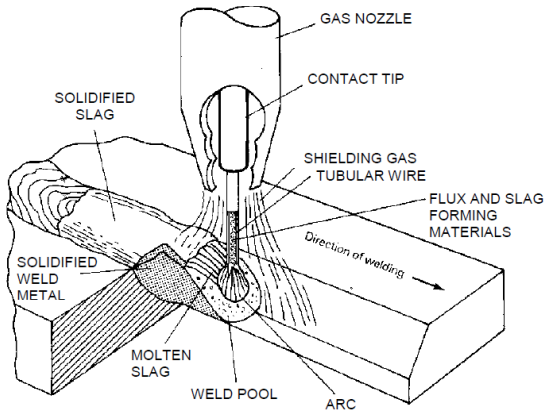

Figure 1: Schematic view of the gas shielded FCAW process (Pitrun, 2004)

The operation of the FCAW process is well illustrated in the figure above, which depicts the interaction between the welding wire, the electric arc, the molten weld pool, and the slag system that forms during welding. As shown in the figure, the consumable electrode used in FCAW consists of a hollow tubular wire filled with flux and slag-forming compounds. When the wire is fed through the contact tip, an electric current passes through it, creating an arc between the end of the electrode and the workpiece surface. This arc provides the thermal energy required to melt both the wire and the base metal, forming a molten weld pool. Surrounding the molten weld pool, the flux contained within the tubular wire decomposes, releasing gases and forming molten slag. These by-products perform several critical functions: the evolved gases contribute

to shielding the weld pool from atmospheric contamination, while the molten slag floats to the surface of the weld pool, protecting the solidifying metal from oxidation and controlling cooling rates. In gas-shielded FCAW, which is shown in figure 1, an external shielding gas—typically CO_2 or an argon-based mixture—is delivered through the gas nozzle to provide additional protection from atmospheric nitrogen, oxygen, and moisture (American Welding Society Handbook, 1991).

As the weld progresses along the direction indicated, the molten pool solidifies to form the weld metal, while the molten slag solidifies above it, creating a protective layer that must be removed between passes. The figure highlights key elements of the process, including the gas nozzle, contact tip, tubular wire, molten slag, weld pool, and the progressive formation of solidified weld metal and slag. These features illustrate the complex thermal, chemical, and metallurgical interactions that occur simultaneously during FCAW. The combination of flux decomposition, external shielding gas, and slag formation not only protects the weld pool but also influences weld bead shape, penetration depth, microstructure evolution, and mechanical properties of the final joint (American Welding Society Handbook, 1991).

Compared with conventional arc welding processes, FCAW offers a number of practical advantages. It can be applied reliably in all welding positions, while still producing sound weld metal that is relatively tolerant of mill scale and less prone to inter-run cold laps than GMAW. FCAW typically provides deeper penetration and higher metal deposition rates than both GMAW and SMAW, and the process generally demands less operator dexterity than GMAW because of its stable, continuous wire feed. In addition, the flux contained in the electrode gives useful metallurgical control, for example through deoxidation and slag formation, which is not available with solid-wire GMAW. These benefits, however, are accompanied by some drawbacks: irregularities in wire feeding can lead to burnback and premature damage of the contact tip; slag formed from the flux must be removed after each pass, increasing post-weld clean-up; and FCAW usually generates more fumes than both GMAW, SMAW and SAW, which may necessitate enhanced fume-extraction and ventilation measures (Pitrun, 2004; American Welding Society Handbook, 1991).

The welding trials in this research were carried out using a six-axis robotic welding system, specifically the CLOOS QRC 350 industrial robot, selected for its high precision, repeatability, and suitability. Robotic welding offers distinct advantages over manual or semi-automatic processes, including consistent travel speed, controlled torch orientation, and highly stable arc

behaviour—factors that are essential when optimizing heat input and managing cooling rates to minimize welding defects and hydrogen-induced cracking (HIC). The QRC 350 integrates seamlessly with CLOOS' advanced QINEO power source, enabling accurate control of wire feed speed, voltage, current, and torch motion through programmable, repeatable paths. This level of control was especially important in this study, as the trial-and-error optimization method relied on the robot's ability to replicate welding parameters with minimal variation while allowing incremental adjustments during parameter development. A representative schematic of the robotic welding setup is provided in Figure 2 to illustrate the system configuration used during experimental work.

Figure 2**.** *Six-axis CLOOS QRC 350 robotic welding system used in this research, source: https://www.exapro.com/cloos-qrc-350-qirox-p250516184/ (assessed 25th November 2025)*

Motivation of Present Work

Flux-Cored Arc Welding (FCAW), introduced in the 1950s, has evolved into a critical welding method, particularly for applications demanding high deposition rates and reliable performance. The use of tubular wires filled with flux provides both shielding gas and slag protection, making FCAW an effective choice for structural steel, stainless steel, and heavy fabrication projects (Minnick, 2010). Its adaptability has driven ongoing research to optimize parameters such as flux composition, filler materials, voltage, and welding speed to meet the increasing demands

of modern fabrication (Jeffus, 2020). Studies also highlight the need for further investigation into FCAW's thermal efficiency, metallurgical impacts, and durability under varying conditions, ensuring continued improvements in weld quality and process efficiency (Gunaraj & Murugan, 2002).

In the context of high-strength steels like HY100, FCAW presents unique challenges. HY100, a steel known for its balance of high tensile strength (100 ksi) and toughness, is widely used in critical applications such as submarine hulls and military vehicles. However, its high alloy content and susceptibility to hydrogen-assisted cracking (HIC) require precise control of welding parameters. While FCAW is not commonly applied to HY100, researchers have explored its potential, noting that challenges such as hydrogen absorption and heat-affected zone (HAZ) brittleness must be addressed (Sadiq et al., 2015). Optimizing parameters like welding current, welding voltage and heat input is essential to maintaining the steel's mechanical integrity during welding.

The welding of HY100 steel has prompted comparisons between optimization methods such as trial-and-error and Design of Experiments (DOE). While DOE provides a systematic framework for studying variable interactions, it can be rigid and less adaptable to the dynamic nature of welding processes. In contrast, trial-and-error optimization offers a flexible, iterative approach that allows for real-time adjustments. This method has proven particularly effective for high-strength steels like HY100, where fine-tuning of parameters such as heat input, welding speed, and filler material is essential to achieve desired mechanical properties, high quality, repeatability and reliability of the process.

For example, the trial-and-error approach can be used to control cooling rates and reduce HIC susceptibility by controlling heat distribution across thicker sections of HY100. This adaptability is especially valuable in high-stakes applications like defense and aerospace, where weld quality must meet stringent standards.

It is worth mentioning to clarify that a DOE framework was not applied in this research. Instead, the study employed an iterative, trial-and-error optimization strategy that was intentionally chosen to complement the robotic welding system used throughout the work. Robotic welding provides a high level of repeatability, precision, and control, but it also highlights subtle variations in heat distribution, arc stability, and bead geometry that are not easily predicted or accommodated within a rigid DOE matrix. Preliminary trials showed that the nonlinear interactions between heat input, cooling rate, wire feed behaviour, and joint configuration in

HY100 steel required continuous real-time tuning that a predefined experimental matrix would have constrained. The trial-and-error method therefore enabled incremental parameter adjustments in response to metallurgical observations and robotic system feedback, while still maintaining systematic documentation, controlled variation, and repeatable conditions. Although not structured as a DOE, this adaptive methodology provided the flexibility necessary to optimize robotic welding performance for HY100 and ensured that the resulting weld quality met the stringent mechanical and reliability requirements expected in critical-service applications.

The potential application of FCAW in welding HY100 steel represents a promising area of research. Addressing challenges like hydrogen cracking, residual stress management, and metallurgical integrity could significantly enhance the efficiency and productivity of FCAW for high-strength materials. Further studies integrating trial-and-error optimization with advanced monitoring techniques could pave the way for broader adoption of FCAW in critical industries, offering improved weld quality and reduced production time.

Contribution to knowledge and practice

Corrosion is a critical factor that significantly impacts the fatigue performance of welded structures subjected to marine environments. Investigations into corrosion fatigue (Ahmad, H.W. et al., 2020; Gkatzogiannis, S. et al., 2021; Jie, Z. & Susmel, L., 2020; Yu, X. et al., 2020; Tan, J. et al., 2021) typically involve deriving S-N curves through testing of specimens that have undergone varying degrees of corrosion. However, there is a paucity of research specifically addressing the comparative fatigue behavior of pre-corroded and non-corroded specimens. This study aims to bridge this gap by conducting systematic fatigue tests on pre-corroded specimens alongside their non-corroded counterparts. This dual approach facilitates a more comprehensive understanding of the effects of corrosion on both the initiation and propagation of fatigue cracks.

A key innovation in the current research is the use of state-of-the-art robotic welding, specifically employing the FCAW process, for specimen preparation. Robotic integration in welding processes offers several advantages, including enhanced consistency in weld quality and improved repeatability over extended durations. This method also introduces flexibility, allowing for more complex welding geometries to be achieved with precision. These benefits are particularly critical for fatigue testing, where weld consistency is paramount to ensure reliable results.

The literature review (Ahmad, H.W. et al., 2020; Gkatzogiannis, S. et al., 2021; Jie, Z. et al., 2020; Yu, X. et al., 2020; Tan, J. et al., 2021; Didonna, G. et al., 2020; Zheng, K. et al., 2020; Zeng, D. et al., 2018; Knysh, V.V. et al., 2018; El Maya, M. et al., 2018; Akita, M. et al., 2018; Wang, X. et al., 2016; Mikkola, E. et al., 2016; Rombado, G. et al., 2016; Taban, E. et al., 2016) highlights a scarcity of data on the fatigue performance of HY100 steel and 316Ti stainless steel in corroded conditions, despite their extensive use in marine and demanding environments. This contrasts with the relatively well-documented fatigue behavior of S355 steel welds, which, however, have been studied without using robotic welding technologies (Gkatzogiannis, S. et al., 2021). By focusing on HY100 and 316Ti weldments and employing robotic FCAW, this study fills a significant research gap and contributes new insights into the corrosion fatigue performance of these materials.

The anticipated outcomes—derived from fatigue experiments, fractographic analyses, and metallographic studies—are expected to substantially enhance the existing knowledge base. By exploring under-studied materials and methods, particularly the implications of robotic FCAW on corrosion fatigue, this research provides novel findings that can inform both academic research and industrial practices. These contributions are especially relevant given the lack of comparable data, emphasizing the importance of this study in advancing the understanding of corrosion fatigue mechanisms in marine structural applications.

Consequently, the baseline knowledge in the field of corrosion fatigue in welded structures, particularly for marine applications, has primarily focused on understanding the degradation of materials under loading conditions and the effects of corrosion on fatigue life. While existing studies have provided valuable insights into the general relationship between corrosion and fatigue, much of the research has been limited to specific materials and welding techniques, and has often overlooked the role of advanced welding methods such as robotic FCAW. Furthermore, the majority of the research has focused on the general effects of corrosion rather than a detailed comparative analysis between pre-corroded and non-corroded specimens under cyclic loading conditions. This study advances beyond the current state of the art by providing a systematic investigation of the fatigue performance of pre-corroded versus non-corroded specimens made from HY100, 316Ti, and S355J2+N steels, specifically using robotic FCAW. The innovative aspect of this research lies in its dual approach to corrosion fatigue testing, which allows for a more accurate understanding of how corrosion affects both the initiation and propagation of fatigue cracks under real-world conditions. By employing robotic welding techniques, this study also introduces a level of precision, repeatability, and consistency in weld

quality that has been previously under-explored, especially in the context of fatigue testing. This contribution significantly advances the field by not only providing new data on the corrosion fatigue behavior of HY100 and 316Ti steels but also by demonstrating how robotic FCAW can be leveraged to produce more reliable and consistent welds for fatigue-critical applications in marine environments. Therefore, this research fills a critical gap in the existing body of knowledge and provides both theoretical and practical advancements, offering a clearer understanding of corrosion fatigue mechanisms and their impact on the design of marine structures.

Organizational Structure of this PhD Thesis

This section outlines the structure of the thesis and briefly summarizes the content of each chapter:

- **Chapter 2** reviews the existing literature and establishes the state of the art in the field.
- **Chapter 3** describes the methods employed in the research.
- **Chapter 4** presents the results and discusses the findings in detail.
- **Chapter 5** reflects on the research goals, evaluates their achievement, and provides a summary of the outcomes. This chapter also includes recommendations for future work.

Chapter 2. Literature Review

This chapter presents a comprehensive review of existing literature to delineate the current state of research in underwater welded structures. The review emphasizes critical aspects such as material selection, welding processes, and strategies for defect mitigation. By synthesizing advancements in materials like HY100 steel and austenitic stainless steel (316Ti), as well as developments in welding techniques such as Flux-Cored Arc Welding (FCAW) and Submerged Arc Welding (SAW), this chapter identifies key trends and challenges in the field.

A primary consideration in the construction of underwater marine systems is the selection of materials that meet specific performance criteria. These include:

- Mechanical Properties: Yield strength, tensile strength, hardness, toughness at low temperatures, ductility, and weldability.
- Corrosion Resistance: High resistance to seawater-induced degradation.
- Environmental Adaptability: Resistance to local environmental factors such as salinity, seawater velocity, temperature fluctuations, and immersion depth, all of which influence corrosion rates.
- Durability and Maintenance: High operational lifespan and minimal maintenance requirements.
- Economic Feasibility: Cost-effectiveness in terms of raw material procurement, maintenance, installation, and removal (Le Mehaute et al., 1990).

Despite the availability of alternative materials like titanium, aluminum alloys, and bronze alloys, steels remain the dominant choice for marine applications worldwide. This preference stems from their cost-effectiveness—being approximately five times cheaper than aluminum—and their extensive usage in shipbuilding, submarine construction, and related fabrications (Le Mehaute et al., 1990; McPherson, 2011). Worldwide, steels continue to be the primary material for these applications. Their well-established performance in existing constructions provides a strong foundation for expanding their use in innovative systems, such as submerged components of Wave Energy Converters and Tidal Energy Converters. In addition to material considerations, the chapter explores the interplay between environmental factors and weldment quality.

Finally, the chapter examines modern strategies for defect mitigation, with a focus on predictive modeling and real-time monitoring techniques. These methodologies, particularly in addressing hydrogen-induced cold cracking (HICC), represent a significant advancement in maintaining the integrity of underwater structures.

Low corrosion resistance is a one of the most important problems which causes qualitative deteriorations and rapid failures of the marine constructions and decreases the human safety. On 10 April 1963 the nuclear submarine USS Thresher was sunk, all crew and shipyard personnel abroad were killed and the radioactive power unit was detected in the floor of the Atlantic Ocean due to the failure of a defective soldered joint in a seawater system (Panayotova et al., 2008). The chemical or electrochemical reactions that occur between the steel and the surrounding seawater are influenced by the seawater temperature, salinity of the seawater, seawater velocity, seawater pH, concentration of dissolved oxygen, marine growth and the bacterial presence, depth of immersion, season of initial immersion, the contact of the marine structure with other materials (e.g. stainless steel, copper, brass or magnetite) and the presence of organic materials (pollution) in seawater (Le Mehaute, 1990; Panayotova, 2008).

An increase of the sea temperature for every 10 ^{o}C will double the corrosion rate of the steel at the initial (electrochemical kinetics – controlled) phase of corrosion (Panayotova, 2008). At the second phase of corrosion, when the process is controlled by diffusion, the solubility of oxygen in seawater is decreased and consequently the corrosion rate is doubled when a rise of 30oC is observed (Panayotova et al., 2008). The relationship between the dissolved oxygen concentration and the corrosion rate is linear. The reduction of the sea salinity (Fig. 1) does not cause reduction in the corrosion rate because it was observed that some steels corroded at greater rates with decreased sea salinity (Panayotova et al., 2008). An increase of the depth of immersion (from 1.5 to 50 m) will increase the corrosion rate about 1.3 times whereas a higher increase of the depth of immersion (from 50 to 500 m) will decrease the corrosion rate (Panayotova et al., 2008). The steel is highly corroded again in water deeper than 500 m and the rate at 5000 m is 1.5 times the rate at 1.5 m (Panayotova et al., 2008). The highest corrosion rate was seen at depth of 2000-5000 m (Panayotova et al., 2008). The average annual corrosion rate for a steel specimen immersed in seawater in winter period was 1.3 – 1.4 times lower in comparison with the respective rate for a steel specimen immersed in summer period (Panayotova et al., 2008). The contact of the marine structure with other materials increases the total corrosion rate because of the contribution of the galvanic corrosion (Panayotova et al.,

2008). The seawater pollution increases St the corrosion rates of the steels (Panayotova et al., 2008; Smith and Howard, 2021).

The corrosion rate (mm/year) of the material is influenced by the previously described environment factors which predominate in the areas under examination. The Aegean Sea basin, which is situated between Greece and Turkey, has a maximum depth of 2568 m, average sea salinity higher than 37 ppt, a surface area of 192,026 km^2 and a volume of 7.4 x104 km^3, whereas the Ionian Sea basin, has a maximum depth higher than 5121 m, average sea salinity higher than 37 ppt, a surface area of 173,493 km^2 and a volume of 10.8 x104 km^3.

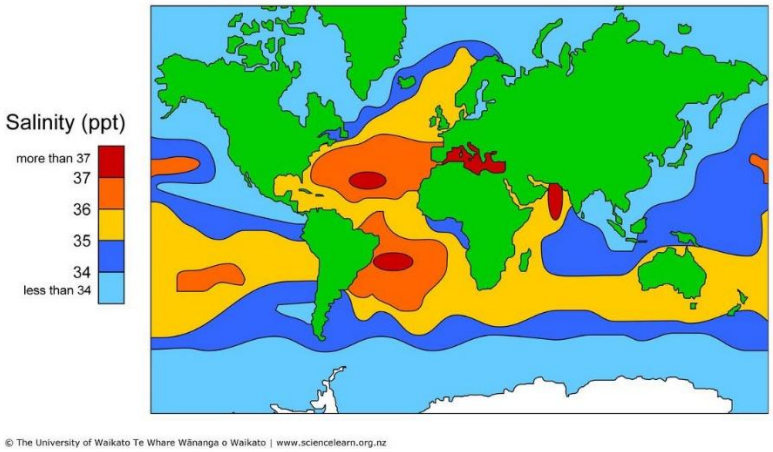

Figure 3: Ocean salinity map. Source: https://brilliantmaps.com/ocean-salinity-map/

The high weldability, and consequently the good welding quality, is influenced by the optimization of various welding parameters (e.g., welding current, welding voltage, welding speed, wire feed speed, shielding gas composition, shielding gas flow rate, etc.). The Welding Procedure Specification is a document that details the joint design, the name of the applied welding process, edge preparation, and all required welding parameters for a specific application, ensuring repeatability by trained and certified welders and operators (American Welding Society, 1987; American Welding Society, 1991).

The welding current, which has a nonlinear relationship with the wire feed speed or melting rate for a specific electrode/wire diameter, composition, and stick-out, influences the deposition rate, penetration depth, and weld bead shape (American Welding Society, 1991; Weman, 2003). Increasing the welding current results in a weld that is higher and narrower with greater penetration depth, while decreasing it reduces penetration, lowers the deposition rate, and produces smaller weld beads (American Welding Society, 1991). Extremely high welding current values can lead to defects such as undercut (a groove melted into the parent metal next to the weld root or toe but not filled with filler metal), porosity, burn-through, and thermal

cracking (American Welding Society, 1987; Weman, 2003). Extremely low welding current values can cause defects like incomplete fusion (lack of complete fusion of filler and base metal) and overlap (excess filler metal extending beyond the weld interface) (American Welding Society, 1987; Weman, 2003).

The welding voltage, defined as the electrical potential between the wire and the workpiece, also impacts weld quality. High welding voltage can result in excessive spatter, undercuts, and non-uniform weld beads, while low welding voltage can lead to inclusions and incomplete fusion (American Welding Society, 1991; Weman, 2003).

The welding speed, which refers to the movement rate of the arc along the joint, determines weld penetration and bead dimensions. High welding speeds result in narrower welds with smaller penetration, whereas low welding speeds increase filler metal deposition per unit length and produce larger weld beads (American Welding Society, 1991). Extremely high welding speeds can cause undercuts, porosity, root imperfections, and magnetic blow effects, while low welding speeds can lead to overlap, excessive spatter, and mushroom-shaped penetration, increasing the risk of thermal cracking and slag inclusions (Weman, 2003).

The electrode/wire stick-out, or extension, is the distance between the end of the contact tube and the electrode/wire tip. A standard value is 10–15 times the electrode/wire diameter (Weman, 2003). Increasing the stick-out raises the electrode's electrical resistance but decreases welding current, wire feed speed, and heat input, while maintaining constant filler metal deposition. This reduces penetration and may result in incomplete fusion (American Welding Society, 1991; Weman, 2003).

The shielding gases are consumables directed by the torch to the arc and weld pool and are used for the protection of the molten metal from oxidation and contamination (American Welding Society, 1991; Weman, 2003). Shielding gases, used for the welding execution, can be grouped into inert gases (i.e., argon, helium), active gases (i.e., carbon dioxide), or a mixture of these gases (American Welding Society, 1991). Helium has 0.14 times higher density than air, while the density of argon is just over 1.4 times that of air (American Welding Society, 1991). The heavier the shielding gas is, the more effective it is for the protection of the welding arc. The suitability of argon for: (a) welding thin materials and materials with lower thermal conductivity, (b) providing reduced penetration, (c) providing cleaning action in aluminum and magnesium welding, (d) being cheap and offering two to three times lower flow rates than helium, (e) providing an easier establishment of the welding arc than helium makes its use as a

shielding gas very frequent because less heat is produced with argon than with helium (American Welding Society, 1991). Helium has a higher thermal conductivity and a higher ionization potential than argon (American Welding Society, 1991). Carbon dioxide (CO_2) is the most widely used shielding gas for Flux Cored Arc Welding process because it is inexpensive and provides higher welding speed and greater joint penetration (American Welding Society, 1991). The heating of the CO_2 to high temperature by the welding arc leads to the dissociation of CO_2 such that carbon dioxide (CO) and oxygen (O) are produced (American Welding Society, 1991). Consequently, a reduction in the filler metal content of elements (silicon, manganese, and titanium) and an increase in carbon is observed (American Welding Society, 1991). The mixture commonly used during the execution of the gas-shielded Flux Cored Arc Welding process is 75% Argon and 25% CO_2. Contamination or presence of humidity in the shielding gas can cause the appearance of spherical or cylindrical porosity (American Welding Society, 1991). The low or inadequate shielding gas flow rate causes the appearance of porosity and contamination of the molten metal, whereas the extremely high flow rate causes turbulence (American Welding Society, 1991).

2.1 Important Materials for Underwater Marine Applications

This section reviews and presents three different steels with low cost which can be used for the improvement of the quality of the already existed welded underwater marine systems and for the construction of underwater marine components.

The physical, chemical, and mechanical properties of the steels are affected by their alloying elements. Hardness, hardenability, yield strength, and tensile strength are increased due to the carbon contents of the steel, whereas weldability, toughness, ductility, and elongation and reduction in area generally decrease with increasing carbon content. Silicon, which is a basic deoxidizer used in steel production, enhances the strength of ferrite without causing a severe loss of ductility. Manganese contents enhance the hardenability and the machinability of steel by forming manganese sulfides but decrease ductility and weldability to a smaller degree than carbon. Increasing phosphorus content increases hardness, yield strength, and tensile strength of the steel but seriously lowers toughness and ductility. Some small additions of phosphorus will enhance the steel's corrosion resistance. Sulfur, which exists in the form of sulfide inclusions, is desirable for the only reason that the machinability of the steel is increased, but it severely decreases weldability, toughness, and ductility of the steel. Chromium additions in

steels increase resistance to oxidation and corrosion and enhance hardenability, hardness, and toughness. Nickel increases toughness, and when it is combined with chromium, it produces steels with improved hardenability and fatigue resistance. Molybdenum additions increase the hardenability of the steels (Reardon, 2011).

Hydrogen-induced cracking or cold cracking or delayed cracking or underbead cracking is the basic defect associated with the welding execution of the three steels (and mainly HY100 sttel) which are presented below. During the welding execution, hydrogen content is unrestrictedly introduced into the molten weld pool from the arc atmosphere, and during cooling, high amounts of hydrogen effuse from the solidified bead, while some others are entrapped into the heat-affected zone of the parent metal. Hydrogen-induced cracking is observed in the heat-affected zone of the parent metal (i.e., the weld toe, the weld root, or in an underbead position) or in the filler metal up to 48 hours, several weeks, or months after the integration of the welding execution (American Welding Society, 1987; Bailey et al., 1973). The locations where hydrogen-induced cracking is observed are illustrated in figures 4 (a) and figure 4 (b).

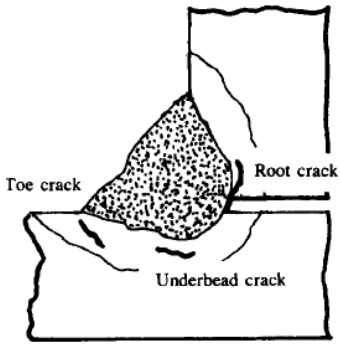

Figure 4 (a): Hydrogen induced cracks in HAZs of fillet welds (Bailey et al., 1973)

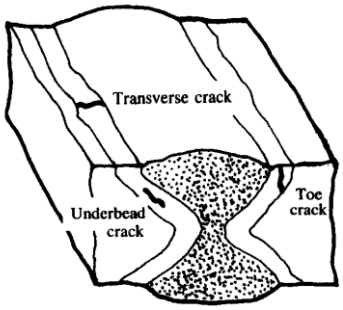

Figure 4 (b): Hydrogen induced cracks in HAZs of fillet welds (Bailey et al., 1973)

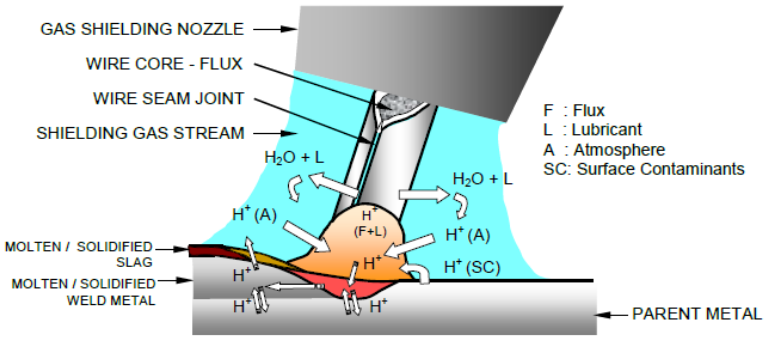

Figure 4 (c): Hydrogen-induced cracking (HIC) mechanism (Pitrun, 2004)

Additional schematic illustrations, such as the one shown in Figure 4(c), greatly assist in understanding the complex interactions that lead to hydrogen-induced cracking during welding. The figure highlights the multiple potential hydrogen sources, including moisture in the atmosphere, adsorbed surface contaminants, lubricants or corrosion products on the filler wire, and decomposition of flux constituents. During welding, these hydrogen-bearing species dissociate under the high temperature of the arc, releasing atomic hydrogen (H). Because of its extremely small atomic radius, hydrogen readily dissolves into the liquid weld pool and diffuses into the surrounding heat-affected zone (HAZ). As the weld metal cools, its solubility for hydrogen decreases dramatically. Hydrogen atoms that were highly soluble in the liquid weld metal become supersaturated in the solidifying microstructure. If the welding parameters, material composition, and cooling rates permit, hydrogen accumulates at microstructural defects such as inclusions, voids, dislocations, and grain boundaries. These hydrogen-rich regions create localised zones of high internal pressure and reduced cohesive strength, significantly weakening the material and increasing its susceptibility to delayed cracking.

Hydrogen cracks, which may be subsurface or may cause failure in the weld surface, can have many variations in length from some microns to several millimeters. Hydrogen-induced cracking is not easily identified because it is observed in a wide range of orientations. In butt welds, heat-affected zone hydrogen cracks are oriented perpendicularly to the weld, but in filler welds, cracks are observed alongside the weld. In the case that hydrogen-induced cracking is observed in the filler metal, it can be transverse or parallel to the weld direction. Transverse cracks have perpendicular or just over a 45° angle to the weld surface (chevron cracks) orientation (American Welding Society, 1987; Bailey et al., 1973).

The appearance of hydrogen-induced cracking is caused by the four following independent factors which must occur simultaneously: (1) Presence of diffusive hydrogen to a noticeable extent in the room air, in welding consumables, and in the surface of the steels to be welded which comes from different sources. The source of hydrogen in the room air is moisture. The

sources of hydrogen in welding consumables are the following: (a) Moisture from the shielding gas, from the flux used during the execution of the Submerged Arc Welding process, or from the flux-cored wires used during the execution of the Flux Cored Arc Welding process, (b) Oil, dirt, and grease present on the surface of welding wires, (c) Rust on the surface of welding wires. The sources of hydrogen from the steels to be welded are: (a) Moisture on the surface of the material to be welded, (b) Fluids used for cleaning the surfaces of the material prior to the welding execution, (c) Oil, dirt, paint, grease, and rust on the surface and nearby the edge preparation. The higher the hydrogen level is, the lower is the resistance to hydrogen-induced cracking formation. (2) Presence of residual stresses on welds, which are usually concentrated at the root and toe of the weld and must not be ignored because stresses are essentially dependent on the size of the weldment, fit-up, external restraint, and the yield strengths of the parent metal and filler metal. (3) A susceptible hardened (i.e., martensitic or bainitic) microstructure in the heat-affected zone of the parent metal which depends on the cooling rate after the welding execution, the composition, and the hardenability of the steel. During the welding execution and the subsequent rapid cooling (quenching), the temperature of the heat-affected zone is higher than one of the adjacent parent metal and a hardened microstructure is caused. (4) Hydrogen-induced cracking is likely to occur in steel plates in temperatures below 250°C because hydrogen cannot diffuse away, and consequently, the toughness of the steel is decreased (American Welding Society, 1987; Bailey et al., 1973).

The methods of the Non Destructive Testing (R. Halmsam, Introduction to the Non-Destructive Testing of Welded Joints), which are executed for the detection of defects in steel weldments are the following:

Visual testing, which is very simple, quick and cheap method used for the inspection of the welds of the steels, can be executed with the aid of a flat or concave mirror, a hand magnifying glass, a small hand lens (magnification 2 – 4x) and the boroscope or intrascope with built – in illumination. Visual testing is applied before the welding execution, during the welding execution and after the welding execution by illuminating the area under examination with light in the visible region. Visual testing is executed before the welding execution by the certified welding inspector in order to check that: (a) the quality and condition of the parent and filler metal is acceptable, (b) the condition of the welding equipment, (c) the shape and the dimensions of the edge preparation are these which are described in the Welding Procedure Specification, (d) the surfaces which are going to be welded are correctly fixed. Visual testing is executed after the welding execution by the certified welding inspector in order to check that:

(a) every welding pass is cleaned before its coverage from the next pass, (b) there are no visible welding defects, (c) check that the arithmetic values of the welding parameters are exactly these which are described in the relative Welding Procedure Specification

Dye or Fluorescent Penetrant methods are methods of Non Destructive Testing where a liquid is put on the surface of the steel weldment and after some time all the welding defects are revealed due to the presence of the liquid.

Magnetic particle testing is an inexpensive and simple method of Non Destructive Testing which is used for the detection of open – to – surface and subsurface cracks in ferromagnetic materials (such as iron, nickel and cobalt alloys) in which the deposited filler metal is also ferromagnetic. The principle of the Magnetic particle testing of non destructive evaluation is that the specimen is magnetized such that magnetic lines of force (magnetic flux) can be produced in the ferromagnetic material. In the case that the magnetic lines of force meet a discontinuity (e.g. crack) the production of secondary magnetic poles at the faces of the crack is observed. The appearance of the magnetic lines of force which are near the surface of the material is executed by the application of magnetic particles such as powder in the U.S.A. or liquid suspension (magnetic ink) in the United Kingdom. The main methods of magnetization are: (a) magnetic flow or magnetic yoke technique in which the specimen is a part of a magnetic circuit by effectively using it as the bridge of a permanent or electromagnet, (b) current flow in which an electric current is passed, broadly along the direction and through the zone where defects are to be expected (c) induced current flow which is not applied in non destructive evaluation of welds and it is only used for ring specimens (d) electromagnetic induction. During the execution of the magnetic particle testing a special preparation on the surface to be inspected is not required but the areas under examination must be dry and free from loose paint, rust, scale, dirt and thin layer of adhesive paint such that the applied liquid suspension is not contaminated. The advantages of the magnetic particle testing method are: (a) its simple equipment, (b) it is a cheap method, (c) its possibility to indicate open – to – surface and subsurface discontinuities, (d) the surface of the material to be tested is not necessary to be ground and polished, whereas the limitations of the magnetic particle testing method are: (a) its restricted application in non – ferromagnetic materials (e.g. austenitic stainless steel), (b) its restricted application if a thick layer of adhesive paint (>50 μm) is present, (c) a high number of tests is required for components of complex shape, (d) the sensitivity of the flaw can vary especially in components of complex shape because of the non uniformity of the magnetic field of the required intensity.

Ultrasonic Testing (Fig. 5) is based on the principle of the introduction of high frequency ultrasonic waves (in the range from 500 kHz to 10 MHz) into the material under examination by manually moving a small probe (the transducer) over the surface of the steel adjustment to the weld and watching a display of the travel time and amplitude of the ultrasonic pulses on an oscilloscope screen. A suitable acoustic coupling medium (water, oil, grease and glycerin) is used between the face of the probe and the surface of the steel such that the high frequency ultrasonic waves are transmitted from the probe into the steel with some attendant loss of energy (attenuation) and they are reflected back from any defect. The same probe or another probe acts as the receiver (transceiver) of the pulse of reflected ultrasound. The detection and the analysis of the reflected ultrasound gives sufficient information about the presence, the location, the possible identification and the size estimation of weld defects. The ultrasonic waves, which are not electromagnetic radiation introduced into the material under examination, have the same characteristics with the sound waves but their essential difference is that their frequency is much higher than the frequency detected by the human ear (i.e. greater than 20 kHz). The wave velocity, which is different in different materials, can be estimated from the relationship: wave velocity (cm/sec)=wavelength (mm)x frequency (MHz). The types of waves used for the ultrasonic flaw detection in steel welds are compressional (longitudinal) and shear (transverse) waves but in some cases surface waves (i.e. Rayleigh, Lamb and Love waves) can be used. Before the execution of the ultrasonic inspection the selected surfaces of the steels to be used for the scanning procedures must be free from weld spatter, loose scale, paint, dirt, machining and grinding particles such that the probe (s) can freely move. The surface roughness must be better than 6 μm RMS for avoiding disturbance of the shape of the ultrasonic beam which could give mistaken about the presence, the location, the possible identification and the size estimation of weld defects.

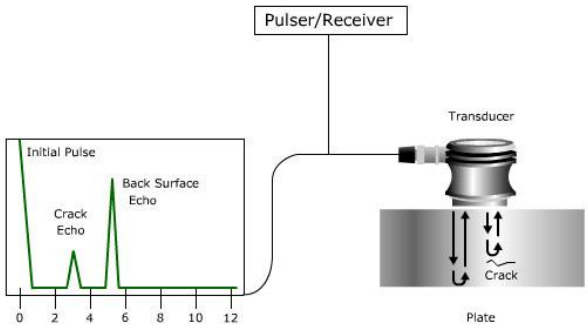

Figure 5: The principle of ultrasonic flaw detection,
Source: https://ndt-kits.com/how-does-ultrasonic-flaw-detector-works/

Radiographic Testing is a method of non-destructive testing where the material under examination for flaw detection is positioned between the source of electromagnetic radiation (X-rays and gamma-rays) and a sheet of photographic film (i.e., the radiograph) or photosensitive paper (American Welding Society, 1987; International Institute of Welding, 1982; Handbook of Radiographic Apparatus and Techniques, 1982). The X-rays and gamma-rays have wavelengths of 2×10^{-12} to 10^{-9} m and 10^{-13} to 2×10^{-12} m, respectively (Handbook of Radiographic Apparatus and Techniques, 1982). The electromagnetic radiation is utilized because it: (a) cannot be reflected or refracted by lenses, prisms, or mirrors, as it normally occurs with visible light, (b) has greater penetration into the material under examination and shorter wavelength than visible light, infrared, ultraviolet (UV), and radio waves, (c) is invisible to the human eye, and (d) travels at the speed of light. Some amounts of the electromagnetic radiation will be absorbed as they pass through the material under examination, some radiation will be scattered, and some radiation will be transmitted through the material onto the sheet of photographic film (American Welding Society, 1987; International Institute of Welding, 1982; Handbook of Radiographic Apparatus and Techniques, 1982).

Higher amounts of radiation will pass through a region of the material under examination where there is a flaw than through solid material, and this essential difference in intensity will be recorded in the sheet of photographic film (American Welding Society, 1987; International Institute of Welding, 1982; Handbook of Radiographic Apparatus and Techniques, 1982). Afterwards, the visual interpretation of the radiographs by positioning them on an illuminated film viewing screen will be executed. The X-rays are produced in a vacuum tube in the form of a glass envelope or metal-ceramic vessel which includes a source of electrons at one end (cathode) and a heavy metal target (anode). The anode consists of a block of copper with satisfactory thermal conduction (American Welding Society, 1987; International Institute of Welding, 1982; Handbook of Radiographic Apparatus and Techniques, 1982). The electrons from the cathode are accelerated towards the anode, generating the beam of X-rays (American Welding Society, 1987; International Institute of Welding, 1982; Handbook of Radiographic Apparatus and Techniques, 1982).

Gamma-rays have high penetration into the material under examination and are generated during the decay of some radioactive materials (radium, uranium, and others) and artificial radioisotopes (International Institute of Welding, 1982; Handbook of Radiographic Apparatus and Techniques, 1982). The artificial radioisotopes mostly used in industry are Cobalt-60 for

thick steel specimens between 50–150 mm and Iridium-192 for thick steel specimens between 10–75 mm. Restricted usage is observed with Cesium-137, Cesium-134, Ytterbium-169, Thulium-170, and Selenium-75 (Handbook of Radiographic Apparatus and Techniques, 1982).

The usage of X-rays and gamma-rays in radiographic testing (RT) has many advantages and disadvantages. X-rays: (a) require large, expensive, and heavy apparatus with significant maintenance needs, (b) depend on an electrical power supply from the mains or a generator, (c) are normally 60° perpendicular to the longitudinal direction of the tube, and (d) are dangerous only during exposure. Gamma-rays: (a) require less expensive apparatus, (b) do not need a power supply, (c) are emitted in all directions, and (d) pose a continuous radiation hazard (American Welding Society, 1987; International Institute of Welding, 1982).

When electromagnetic radiation interacts with the material, the amount transmitted to the radiograph can be estimated by the equation

$$I = I_0 e^{-\mu t},$$

Where I_0 is the intensity of the incident beam, I is the intensity of the transmitted beam, e is the base of the natural logarithm, μ is the linear absorption coefficient, and t is the thickness of the material (Handbook of Radiographic Apparatus and Techniques, 1982).

The advantages of radiographic testing include: (a) applicability to different material types, (b) detection of surface and subsurface defects, (c) portability and cost-effectiveness of gamma-ray equipment compared to X-ray equipment, and (d) the film's use as a permanent record of weld quality. The disadvantages include: (a) the hazardous nature of electromagnetic radiation, (b) high equipment costs for thick ferrous materials (>150 mm), (c) expensive X-ray machines, isotopes, and licensing, and (d) difficulty detecting laminations in plates (International Institute of Welding, 1982; Handbook of Radiographic Apparatus and Techniques, 1982).

HY 100 steels

HY 100 is a 100,000-psi high-yield strength quenched and tempered fully killed with a good combination of strength and toughness, which is used for submarine constructions and has many industrial applications in pressure vessels (Flax et al., 1971; Gabler, 2000). The basic advantages of the HY steel materials are their excellent resistance to underwater explosion shocks and their good weldability in heavy thicknesses with little preheat or no post-weld heat

treatment (Patel and Kumar, 2022). The chemical analysis of the HY 100 steel is presented in Table 1 (Flax et al., 1971).

Table 1: Chemical Compositions of HY 100 steel parent metal. Source: Flax et al. (1971).

Element (wt%)	C	Si	Mn	P	S	Co	Cr	Ni	Mo	Ti	Va
MIL-S-16216	0.20 Max.	0.15 - 0.35	0.10 - 0.40	0.025	0.025	0.25	0.02	2.25 - 3.50	0.20 - 0.60	0.02	0.03

Taking into consideration the industrial experience, it is observed that the HY 100 steels are welded with specific fusion welding processes such as the Shielded Metal Arc Welding, Submerged Arc Welding, Gas Metal Arc Welding, and Flux Cored Arc Welding (Flax et al., 1971). Flux Cored Arc Welding and Submerged Arc Welding are presented below because they are more advantageous welding processes compared with the others (Kumar and Singh, 2022).

Flux Cored Arc Welding process is a semi-automatic or automatic arc welding process in which the heat required to melt and weld the material is produced by the establishment and maintenance of an electric arc between the tip of a continuously fed consumable filled with a flux and the workpiece (American Welding Society, 1991). This process has the same equipment as the Gas Metal Arc Welding process, but the generally higher values of welding currents used with cored filler wires require power sources with higher capacity (American Welding Society, 1991). Flux-cored welding wires provide high deposition rates and have higher resistance to draughts than metal arc electrodes. The fume produced from the usage of flux-cored welding wires is higher than the one produced from the usage of metal arc electrodes.

The advantages of this process are: (a) resistance to cracking defects, (b) excellent smooth and uniform weld appearance, (c) high deposition rate, which is four times greater than the deposition rate created by Shielded Metal Arc Welding, (d) ability to be used for welding a wide range of thicknesses in many types of steels, (e) illustrating eliminated distortion compared with the Shielded Metal Arc Welding process, (f) high operator factor, and (g) the cleaning required before the welding execution is less than that required in Gas Metal Arc Welding. The limitations of this process are: (a) restriction to welding ferrous metals and nickel-based alloys, (b) the need for removing the slag covering the passes, (c) the fumes and smoke produced in Flux Cored Arc Welding are higher than those produced in Gas Metal Arc Welding

and Submerged Arc Welding, and (d) more maintenance of the equipment is required because of the complexity of the equipment (American Welding Society, 1991).

Submerged Arc Welding process is a semi-automatic, automatic, or mechanized arc welding process in which the heat required to melt and weld the steel plates is generated by the initiation and maintenance of an electric arc between the tip of a continuously fed filler wire and the workpiece. This process can be used in pipe welding, shipbuilding, heavy structural steelwork, and general fabrications (American Welding Society, 1991; Weman, 2003). The Submerged Arc Welding process is schematically illustrated in Figure 6, and the utilized welding current ranges between 350 A and 2000 A (American Welding Society, 1991; Weman, 2003; Norrich, 2006). This process does not utilize a shielding gas but rather a granulated mineral flux for the stability of the welding arc, for the control of the chemical and mechanical properties of the final weld deposit, and for the protection of the welding zone from atmospheric contamination (American Welding Society, 1991; Weman, 2003; Norrich, 2006).

The different types of fluxes are fused, bonded (also known as agglomerated), and mechanically mixed (American Welding Society, 1991; Weman, 2003). The preparation of fused fluxes includes melting and dry-mixing the raw ingredients at high temperature in an electric furnace, such that a glass-like mass is generated. This mass is permitted to cool, and is afterward broken up, screened to suitable grain sizes, and packaged. Fused fluxes must have good chemical homogeneity and must not be hygroscopic (American Welding Society, 1991; Weman, 2003). The composition of fused flux is not affected because the fines can be easily removed. The preparation of bonded fluxes includes powdering, dry-mixing, and bonding or sintering the raw material with a binder (potassium silicate, sodium silicate, or a mixture of these two) in a rotary kiln at a temperature of 600–900°C (American Welding Society, 1991; Weman, 2003). Then the material is broken up, screened to suitable grain sizes, and packaged. Bonded fluxes are unfortunately hygroscopic and have relatively low grain size. The preparation of mechanically mixed fluxes includes mixing two or more fused or bonded fluxes in any ratio such that the desirable results are accomplished.

The advantages of this process are its high weld quality, high melting and deposition rates, deep penetration, and automatic operation, whereas the limitations of this process are the difficulty of welding in any position, the invisible arc radiation, the relatively high equipment cost, and its suitability for materials with thicknesses higher than 6 mm (American Welding Society, 1991; Weman, 2003; Norrich, 2006).

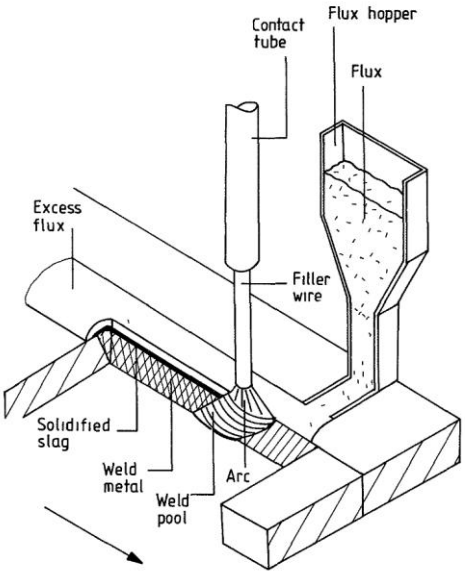

Figure 6: Schematic View of Submerged Arc Welding Process. Source: Norrich, 2006.

X6CrNiMo17-12-2 (316Ti) stainless steel

The X6CrNiMo17-12-2 (316Ti) austenitic stainless steels are steels with titanium stabilization, the nominal chromium content higher than 16%, and an excellent notch toughness at cryogenic temperatures (American Welding Society, 1998). The principal advantages of 316Ti steels are their higher corrosion and oxidation resistance than the standard grades of 316, their better ductility and toughness than carbon and alloy steels, and their good maintenance at elevated temperatures for a longer period without the presence of precipitation taking place (American Welding Society, 1998; Brnić et al., 2011). Austenitic stainless steels, including 316Ti, retain high toughness down to cryogenic temperatures (≈ −196 °C), as the austenite phase does not undergo a ductile-to-brittle transition (Davis J.R., 1994; ASM International, 1994).

The immersion of the 316Ti steel sample in boiling 42% magnesium chloride ($MgCl_2$) solution can indicate the likelihood of appearance of transgranular or intergranular stress corrosion cracking (SCC) in the 316Ti steel (American Welding Society, 1998). SCC is caused by the simultaneous subjection of the 316Ti steel to tensile stress and its exposure to one specific corrosive medium, such as caustic or chloride solutions (Le Mehaute & Hanes, 1990). The resistance of the 316Ti to pitting corrosion is significantly affected by the surface treatment (Fajnor et al., 2010). The chemical analysis of this steel is presented in Table 2 (Fajnor et al., 2010).

Noga et al (2020) investigated how different welding methods (GTAW, GMAW, EBW, PAW) influence the microstructure and mechanical properties of AISI 316Ti stainless steel. The study found variations in the microstructure, particularly in the delta ferrite content and grain formation within the welds. GTAW and PAW welds showed the highest levels of delta ferrite, which can enhance corrosion resistance, while EBW welds exhibited the lowest delta ferrite content, suggesting finer precision. The mechanical testing revealed that GMAW achieved the highest tensile and yield strengths, making it the most robust technique among those studied. In contrast, PAW welds had lower strength values, which may limit their use in applications demanding high mechanical performance. Despite its lower mechanical properties, PAW and GTAW welding contributed to improved corrosion resistance due to their higher delta ferrite content. This research highlights the need to balance mechanical strength and corrosion resistance when selecting welding techniques for the industrial use of AISI 316Ti stainless steel.

Table 2: Chemical Compositions of X6CrNiMo17-12-2 parent metal. Source: Fajnor et al. (2010).

Element	(wt %)
Carbon	0.04
Silicium	0.43
Manganese	1.69
Phosphor	0.026
Sulphur	0.002
Nitrogen	0.012
Chromium	16.5
Nickel	10.6
Molybdenum	2.12
Titanium	0.41
Vanadium	0.003

S355J2N steel

S355J2N is a hot-rolled normalized structural steel with a minimum yield strength of 355 N/mm², which has many common applications due to its excellent mechanical properties. The chemical analysis of this steel is presented in Table 3 (Plum, 2015).

Table 3: Chemical Compositions of S355J2+N parent metal. Source: Plum, 2015.

Element (wt %)	Material thickness (6 mm)	Material thickness (14 mm)
Carbon	0.17	0.15
Silicium	0.02	0.31
Manganese	1.59	1.41
Phosphor	0.011	0.014
Sulphur	0.011	0.014
Nitrogen	0.004	0.005
Aluminum	0.028	0.037
Copper	0.03	0.04
Chromium	0.02	0.06
Nickel	0.03	0.02
Molybdenum	0.001	0.005
Niobium	0.001	0.003
Titanium	0.001	0.003
Vanadium	0.003	0.004

2.2 Flux Cored Arc Welding Process

Flux-cored arc welding (FCAW) was introduced in the early 1950s as a versatile process to address industrial demands for efficient and high-quality welding methods. The development of gas-shielded FCAW (FCAW-G) in 1957, followed by self-shielded FCAW (FCAW-S) in 1960, significantly expanded its applications in industries such as construction, shipbuilding, and heavy fabrication. Over the last two decades, FCAW has been the subject of extensive research aimed at improving commercial electrodes, understanding the role of shielding gases,

controlling diffusible hydrogen levels, optimizing welding consumables, refining welding sequences, and studying fatigue behavior in various materials.

Initially, FCAW relied on an AC welding system utilizing large electrodes, largely due to economic considerations. However, advancements in technology and materials have shifted the preference to DC welding systems, which employ finer electrodes. This shift has resulted in improvements in weld quality, usability, and overall process efficiency.

The role of shielding gases in FCAW has been extensively investigated, given their critical function in protecting the weld pool from atmospheric contamination by oxygen and nitrogen. While the properties of the weld metal are primarily influenced by the composition of the consumable electrode, the choice of shielding gas plays a significant role in determining the weld's strength, ductility, toughness, and corrosion resistance. Studies indicate that shielding gases with high oxidation potential, such as oxygen or carbon dioxide, tend to reduce weld strength and toughness (Lee and Park, 2020) by increasing oxide inclusions and decreasing essential alloying elements like manganese and silicon. Furthermore, variations in shielding gas composition have been shown to influence weld bead geometry, arc stability, and overall weld quality.

Recent research has focused on developing advanced electrode designs and optimizing shielding gas mixtures to enhance weld performance and efficiency. For instance, modern studies emphasize tailoring gas compositions to achieve desired mechanical properties while minimizing defects. These advancements underscore FCAW's continued evolution and its ability to meet the demands of modern fabrication industries (Parmar, 1992; Morigaki et al., 1976).

The role of shielding gas compositions in flux-cored arc welding (FCAW) significantly influences key factors such as arc stability, deposition rate, microstructure, and the chemical and mechanical properties of welds, particularly in mild carbon steels. Research has shown that increasing the CO_2 content in argon–CO_2 mixtures reduces weld metal ferrite content and influences the overall weld quality (Lathabai et al., 1985).

A study by Arivazhagan et al. (2009) evaluated four shielding gas compositions—pure argon (Ar), pure CO_2, 80% Ar + 20% CO_2, and 95% Ar + 5% CO_2—and concluded that a 95% Ar + 5% CO_2 mixture provided the best combination of toughness and process performance for FCAW. Similarly, experiments with commercially available flux-cored wires demonstrated that

increasing CO_2 in the shielding gas increases oxygen levels in weld metals, which decreases the recovery of essential alloying elements like manganese and silicon. These changes were associated with harsher arcs, higher spatter, and altered weld bead geometry, including increased convexity and penetration. Heat input further compounded these effects, producing inconsistent trends in Charpy impact toughness (Lathabai & Stout, 1985).

Further investigations into the impact of shielding gas compositions, such as those by Gadallah et al. (2012), revealed strong links between gas composition and metallurgical transformations, influencing weld strength, ductility, and corrosion resistance. The choice of shielding gas also affects arc stability and the transfer mode of metal deposition, as established by Zielińska et al. (2009), who demonstrated that oxidation-reduction reactions during welding dictate transitions between spray-arc and globular transfer modes.

In addition to shielding gas studies, research into hydrogen management in FCAW welds has highlighted its critical role in preventing weld defects. Diffusible hydrogen, often introduced through moisture in the flux, atmospheric contamination, or flux residues, remains a primary cause of cold cracking in steel welds. Bracarense et al. (2002) found that increasing welding current correlates with higher diffusible hydrogen levels in weld deposits. Their study utilized gas chromatography and advanced imaging to quantify these effects, demonstrating a linear relationship between current increases and hydrogen absorption.

Several experimental studies have also explored the influence of input-output relationships in welding parameters, such as arc voltage, feed rate, and heat input, on weld quality. For example, Pang et al. (2011) analyzed hardness variations in heat-affected zones (HAZ) during submerged arc welding and verified the results using weld thermal cycle simulations. Similarly, finite element modeling of gas metal arc welding (GMAW) processes has provided valuable insights into residual stress and solidification behaviors during welding (Choi et al., 2002).

These findings collectively underscore the importance of precise control over shielding gas compositions and welding parameters to optimize weld quality and mechanical properties. Advanced methodologies, such as mathematical modeling, thermomechanical simulations, and experimental evaluations, continue to drive innovations in FCAW, ensuring its adaptability to modern industrial requirements.

Weldment quality

The evaluation of welded structures necessitates a thorough assessment of factors such as joint integrity, mechanical properties, and resistance to corrosion. Structural steels, particularly high-strength materials like HY100, face unique challenges, including various failure modes that can compromise their structural integrity. Among these, hydrogen-induced cold cracking (HICC) is of greatest concern, requiring meticulous process controls to prevent its occurrence. Historically, HICC was a significant obstacle to the adoption of HY80 steel in U.S. Navy shipyards due to its high susceptibility. This type of cracking typically arises from a combination of factors, including hardened microstructures in the heat-affected zone (HAZ), elevated hydrogen concentrations in the HAZ, tensile stresses, and environmental conditions such as ambient temperature (Kiefer et al., 2020; TWI, 2023). Figure 1 illustrates the microstructure of HY100 steel, highlighting its bainite and martensite phases, which contribute to its high strength and susceptibility to hydrogen-induced cracking.

Hydrogen Sources in Welding

The sources of hydrogen that negatively affect weldment quality have been systematically categorized into the following groups:

- **Moisture in shielding gases.**
- **Organic materials and absorbed moisture in flux-cored wires.**
- **Contaminants, such as oils and rust, on the base material.**
- **Atmospheric moisture and other environmental factors** (Harvig et al., 1999; Sierdzinski et al., 2022).

Research has demonstrated that modifying flux compositions can significantly reduce hydrogen absorption during welding (Sierdzinski et al., 2022). Harvig et al. (1999) found that environmental moisture during electrode storage exacerbates hydrogen levels in weld deposits. Even when electrodes were stored under controlled conditions, long-term exposure to ambient air resulted in elevated diffusible hydrogen levels in the welds.

Influence of Welding Parameters

Several welding parameters play a critical role in influencing diffusible hydrogen content:

- **Welding Current and Voltage:** Elevated welding current and voltage correlate with higher diffusible hydrogen levels. Studies by White et al. (1992) and Kurokawa et al. (2019) showed that increasing current from 160A to 260A when using rutile flux-cored wires resulted in higher hydrogen absorption. This trend was consistent across different wire diameters and shielding gas compositions.
- **Shielding Gas Composition:** The composition of shielding gases significantly affects arc stability, weld penetration, and hydrogen absorption. Gases like pure CO_2 are particularly effective at controlling hydrogen levels, even under humid conditions (Kiefer, 2020; Francis et al., 2021).
- **Preheating and Interpass Temperatures:** Proper preheating and controlled interpass temperatures mitigate rapid cooling rates, which reduces the formation of brittle microstructures in the HAZ. This practice lowers the likelihood of hydrogen entrapment (Kisney et al., 2018).

Key Findings on Mitigation

Recent studies have identified critical methods to mitigate hydrogen-induced cracking:

1. **Electrode Design:** The use of low-hydrogen consumables, such as basic flux-cored wires, significantly minimizes hydrogen content in weld deposits. Advances in flux formulations have further enhanced this effect (Kuebler et al., 2021).
2. **Heat Input Management:** Studies indicate that heat input profoundly impacts diffusible hydrogen levels. Basic wires demonstrate less sensitivity to heat input variations compared to rutile wires, making them more suitable for critical applications (Pitrun et al., 2022).
3. **Preheating and Interpass Control:** Research by Lee et al. (2019) and Kisney et al. (2018) highlights the effectiveness of maintaining appropriate preheating and interpass temperatures. These measures reduce the susceptibility to hydrogen-induced cracking by softening the weld metal and preventing martensitic transformations.

Emerging Research Directions

Recent advancements have focused on real-time monitoring and predictive modeling to optimize welding parameters. Machine learning algorithms are being used to predict diffusible hydrogen content based on real-time process variables such as heat input, shielding gas

composition, and electrode type (Rahman et al., 2023). Additionally, innovations in shielding gas technology are exploring novel blends to enhance arc stability while minimizing hydrogen absorption.

These emerging strategies promise to refine welding processes, ensuring higher-quality weldments and reducing defect rates, particularly in critical applications requiring structural integrity and longevity.

Chapter 3. Material and methods

This chapter outlines the materials, experimental setup, and methods employed in this study to investigate the welding and corrosion resistance of HY100, 316Ti, and S355J2+N steels using the Flux-Cored Arc Welding (FCAW) process. The experiments were designed to determine optimal welding parameters, evaluate corrosion resistance, and assess performance under varying material configurations and environmental conditions. Each phase of the research—ranging from parameter optimization to long-term failure performance testing—was meticulously executed to ensure the reliability and applicability of the findings in high-demand industrial contexts.

During this study, the following experiments were performed:

1. **Determination of optimum welding parameters in welded specimen with 15 mm thickness:**
   This phase involved a trial-and-error approach using trial specimens to identify defect-free parameters. Multiple trial specimens were used, and non-destructive testing (NDT) methods (e.g., visual inspection, ultrasonic testing) were applied to refine these parameters iteratively. Once optimized, these parameters were used to weld actual specimens to validate consistency and repeatability.

2. **Repetition of Welding with 10 mm Thickness:**
   A second round of experimentation replicated the welding process using 10 mm thick specimens**.** This phase validated whether the optimized parameters were applicable to a different material configuration.

3. **Corrosion resistance testing:**
   This experiment involved three welded steel specimens (HY100, 316Ti, S355J2+N) subjected to the Salt Spray Test as per ASTM standards. Corrosion resistance was assessed through parameters like mass loss and corrosion rate, alongside optical microscopy and SEM analyses for morphology characterization.

4. **Corrosion Resistance Failure Performance Testing**:

This phase further evaluated the failure performance of the welds under long-term or harsher conditions. The testing extended beyond standard corrosion resistance to assess mechanical integrity under extended or intensified corrosive environments.

Flux-Cored Arc Welding FCAW

All welding experiments were robotically executed with the aid of Flux Cored Arc Welding (FCAW) process (Mohamat, Ibrahim, Amir, & Ghalib, 2012). FCAW process is a semi-automatic or automatic arc welding process in which the heat required to melt and weld the material is produced by the establishment and maintenance of an electric arc between the tip of a continuously fed consumable filled with a flux and the workpiece (American Welding Society [AWS], 1991).

The experimental plan, procedure, and methodology adopted in this research concentrated on the implementation of a trial-and-error approach for the FCAW process to evaluate its impact on the soundness and quality of welded joints, which subsequently affects other important characteristics such as weld bead geometry, metallurgical characteristics, and mechanical properties of the welded joints. Usually, for sufficient welding process control and optimization, the Design of Experiments (DOE) techniques are utilized. However, in the case of HY100 steels, the trial-and-error approach was selected because this approach is particularly suited to detecting the optimum parameters that cause zero defects.

The trial-and-error approach is particularly beneficial for the robotic FCAW process of HY100 steels. According to the literature review, there has been a lack of previous research in this area. According to the literature, research in this area is limited. This approach allowed for fine-tuning specific welding parameters for materials, thicknesses, and configurations often used in high-demand applications, such as aerospace and submarine constructions. Critical parameters, including welding current, welding voltage, and welding speed, were identified and adjusted iteratively to achieve weldments of superior quality. For specific values of these parameters, flaw-free welds were achieved. Mechanical testing, including tensile strength, yield strength, and fatigue strength (in corroded and non-corroded specimens), was then conducted to evaluate the weld quality.

Metallurgical analysis was performed on the base metal, heat-affected zone (HAZ), and weld metal, using optical and scanning electron microscopy (SEM). The study also emphasized

fatigue performance under marine conditions to assess the long-term durability of the welds. This iterative optimization process ensured welding parameters were adjusted to meet specific application demands, providing a robust framework for achieving high-quality welds in industrial applications.

Materials and Experimental Setup

For this research, HY100, 316Ti, S355J2+N steel plates with a thickness of 15 mm and 10mm were selected as the base material due to their mechanical properties and suitability for high-demand applications. The welding process was supported by a robotic system from CLOOS using the Quineo Pulse 600 welding machine. A single V edge preparation was performed at an angle of 60° to ensure optimum penetration and weld strength.

The filler material used was a flux-cored wire (diameter: 1.2 mm) selected for its compatibility with the three materials (HY100, 316Ti, S355J2+N). The shielding gas composition was 82% argon and 18% carbon dioxide, with a flow rate of 16 litters per minute, providing stable arc performance and protection from atmospheric contamination. Before applying the final welding parameters, trial values were tested on identical specimens. Each trial weld underwent visual inspection and magnification to identify defects related to specific parameter values.

Parameter optimization

Non-destructive examinations, including **visual inspection, magnetic particle inspection, liquid penetrant inspection, radiographic inspection, and ultrasonic inspection**, were conducted on trial specimens after 30 days to monitor for hydrogen-induced cracking. Adjustments to welding parameters continued until defect-free welds were achieved. Once the trial specimens met quality standards, the optimized parameters were used to weld the actual specimens, ensuring process consistency and repeatability. The actual specimens were also inspected with the previously mentioned non-destructive examination methods.

The heat input, which is a relationship between the welding current, the welding voltage, and the welding speed, is given from the following equation (AWS, 1991):

$$HI\ (\frac{KJ}{cm}) = \frac{V\ (A) \cdot I\ (A) \cdot 60}{1000 \cdot WS\ (cm/min)}$$

Where I is the current (A), V is the voltage (V), WS stands for the welding speed (cm/min), and HI is the heat input (KJ/cm). Final parameters, including welding current, welding voltage, and welding speed, were adjusted to ensure defect-free welds with consistent mechanical properties.

The output of this research highlights the practical advantages of trial-and-error over rigid DOE frameworks in certain applications and provides valuable insights into the behavior of HY100 and AISI 316Ti steels under the FCAW process. The iterative optimization approach ensured that welding parameters could be fine-tuned to meet specific application demands, making it a robust strategy for achieving high-quality welds in industrial contexts.

It is obvious from the relative references (Mohamat et al., 2012) that the welding parameters which mostly affect the quality characteristics of the welded joints and play a significant role during the FCAW process are the welding current, the welding voltage, and the welding speed, and for this reason, they were selected as dominant during the experimental execution.

Before the beginning of the welding experimental execution, all steel plates were cleaned with the aid of shot blasting. FCAW operations were performed with the aid of a welding robot. Welding experimental execution between dissimilar steels was not investigated during this study. The arithmetic values of the parameters such as thickness (i.e., 15 mm) and length (i.e., 300 mm) of each specimen, shielding gas, shielding gas flow rate, edge preparation (i.e., single V-butt joint preparation with 60° induced angle) of the welded joint, preheating temperature, and interpass temperature were kept constant during the experimental execution, whereas the arithmetic values of the welding current, welding voltage, and welding speed were changed. In each experiment, all arithmetic values for each welding parameter and the number of welding layers for each welded specimen were recorded.

After the integration of the welding experimental execution, the welded joints of the HY100 steel specimens and the welded joints of the S355J2+N steel specimens were inspected with the aid of Visual Testing, Magnetic Particle Testing, Ultrasonic Testing, and Radiographic Testing, whereas the welded joints of the 316Ti stainless steel specimens were inspected with the aid of Visual Testing, Liquid Penetrant Testing, Ultrasonic Testing, and Radiographic Testing (Halmsam, 1996). All welded defects which are described in Table 1 were recorded, and the specifications (ISO 5817, 2014), which describe the acceptance and unacceptance criteria of the welding defects for fusion welded joints, were implemented.

Table 4: Classification of welding defects in butt welds. Source: ISO 5817 (2014)

Imperfection designation
Porosity
Undercut
Incomplete fusion (Lack of fusion)
Incomplete root penetration
Crack
Crater crack
Incomplete root penetration
Excess penetration
Excess weld metal
Overlap
Burn through
Inclusions
Spatter
Stray arc
Root concavity
Shrinkage cavity

After the integration of the non-destructive evaluation of the welded steel specimens, the preparation of the metallographic specimens was conducted in accordance with the specification ASTM E3-11 (2017). The welded specimens were mechanically cut perpendicular to the welding direction with the aid of a saw, grinded, and polished through a series of metallographic papers until the desirable surface finish has been accomplished. The primary objective of metallographic examinations of the welded specimens is the revelation of the metallurgical structure in the parent metal, in the filler metal, and in the heat-affected zone in accordance with the iron-iron carbide phase diagram with the aid of a light optical or scanning electron microscope (AWS, 1987; ASTM E3-11, 2017). Macroscopic examination was used to

determine the number of welding layers, whereas microscopic examination was used to determine excessively small imperfections at magnifications of about 50 times or higher (AWS, 1987). The welded specimens were etched with the suitable etchant in accordance with the specification ASTM E407 (2015) such that the regions of the parent metal, filler metal, and HAZ were revealed.

Corrosion Resistance Evaluation

The experimental investigation of the corrosion resistance of three different welded steel specimens was executed using the Salt Spray Test. The Salt Spray Test is a well-known accelerated test method used for evaluating the corrosion resistance of various materials (e.g., painted or coated materials, electrical connectors) subjected to controlled corrosive environments (ASTM B117, 2018; EIA 364-26, 2014). Generally, the most common specifications for the Salt Spray Test are ASTM B117 (2018), MIL-STD-810H (2019), and ISO 9227 (2017). The apparatus (see Fig. 7) required for salt spray (fog) exposure consists of a fog chamber/cabinet, a reservoir with salt solution, a compressed air supply, one or more atomizing nozzles, suitable supports for positioning the welded specimens, a chamber heater, and necessary means of control (ASTM B117, 2018).

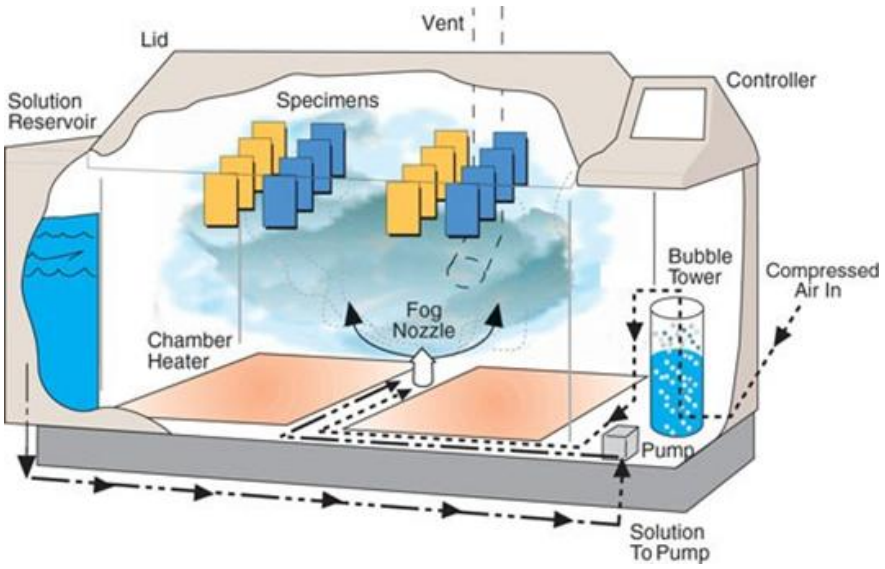

Figure 7: Schematic view of Salt Spray (Fog) Apparatus, source: https://www.pfonline.com/articles/understanding-corrosion-and-salt-spray (accessed 28th November 2024).

The HY100 welded steel specimen, the 316Ti austenitic stainless welded steel specimen, and the S355J2+N welded steel specimen with the optimum weld quality were selected for the Salt Spray Test. The test was performed in accordance with ASTM B117 (2018), and the assessment of the corrosion damage of each welded specimen was executed following ASTM G1 (2017).

All three welded steel specimens with optimum weld quality, which had the same edge preparation (i.e., single V-butt joint preparation) and the same thickness (i.e., 15 mm), were positioned in the salt spray chamber using a special welded plastic (PVC) fixture at an angle of 45° to ensure unencumbered exposure to the fog. The exposed areas of the specimens included the weld face and the parent material. Contact between the specimens was avoided, and the salt solution from one specimen did not drip onto another (ASTM B117, 2018). During the Salt Spray Test, a solution of 5% sodium chloride (NaCl) was used to create a highly corrosive environment, following ASTM B117 (2018). The exposure period of the welded specimens in the salt spray chamber was 300 hours, and the temperature was maintained at 35°C (95°F). After 24, 48, 72, 96, 168, 192, 216, 240, and 264 hours of exposure to the controlled corrosive environment, the mass (grams) of each welded specimen was measured without removing the salt deposits.

After 300 hours of exposure, the welded specimens were washed in clean running water not warmer than 38°C (100°F) to remove the salt spray deposits and corrosion products from their surface and immediately dried in accordance with ASTM B117 (2018). Subsequently, the mass loss of corroded material and the corrosion rate of each welded specimen were calculated following ASTM G1 (2017). The corrosion morphology of each welded specimen was further analyzed using Optical Microscopy and Scanning Electron Microscopy (SEM). Metallographic analysis was conducted on transverse cross-sections prepared from all examined specimens. Standard metallographic techniques, including grinding and polishing, were applied, followed by etching. The etchant used was Nital 5% for the S355J2+N and HY100 steels, and Marble's reagent for the 316Ti steel.

The selection of a 300-hour exposure period for the salt spray test was relied on both the standardised framework of ASTM B117 and precedent in corrosion-fatigue research. Although ASTM B117 does not prescribe a specific duration, it emphasises that test duration must be chosen so that measurable corrosion effects develop. In comparative studies of corrosion-fatigue behaviour, durations of hundreds of hours have been employed; for example, one recent investigation used 12-month salt spray exposure (~8 760 hours) to examine welded joints in a marine-like environment and observed marked fatigue strength reduction as a result of the prolonged exposure (Shojai et al, 2025). While such long durations represent extreme accelerated ageing, shorter exposures—typically ranging from 96 to 500 hours—are frequently used for initial corrosion screening of materials and coatings. Therefore, the 300-hour period

was selected as a compromise that is sufficiently long to produce relevant corrosion damage (including pitting, surface attack and weld-zone degradation) yet not so long as to risk excessive specimen loss or remove relevance to realistic structural exposure. This duration ensures that the corrosion processes meaningful for fatigue initiation and propagation in welded steel specimens (HY100, 316Ti and S355J2+N) are captured, while maintaining alignment with literature practices and preserving specimen integrity for subsequent mass-loss, microscopy and metallographic analyses.

The comprehensive methodology described in this chapter ensured meticulous preparation and execution of experiments to investigate the welding and corrosion resistance of HY100, 316Ti, and S355J2+N steels. The application of optimized Flux-Cored Arc Welding (FCAW) parameters and rigorous testing protocols provided robust datasets for analyzing the mechanical properties, microstructural characteristics, and corrosion performance of the welded specimens. The following chapter presents the results obtained from these experiments, along with a detailed discussion to interpret their significance and implications for industrial applications.

Chapter 4. Results and Discussion

This chapter presents the findings of the experimental investigation, focusing on the welding quality, mechanical properties, and corrosion resistance of HY100, 316Ti, and S355J2+N steels. The results are discussed in relation to the optimized welding parameters, with particular emphasis on the effects of welding current, voltage, and speed on defect formation and material performance. Additionally, the corrosion resistance and failure performance under accelerated testing conditions are analyzed to evaluate the suitability of these materials for demanding industrial environments.

The optimum arithmetic values of the HY 100 steel welded joints are presented in table 5. The optimum arithmetic values of the 316Ti steel welded joints are presented in table 6.

Table 5: Optimum weldability of HY 100 welded steel specimens at 15 mm thickness

Welding layer	Current (*I*)	Voltage (*V*)	Welding speed (cm/min)	Heat input (KJ/cm)	Presence of welding defects
1	186	26.2	15	19.49	no defects
2	230	25.9	28	12.77	no defects
3	232	23.7	35	9.43	no defects
4	232	23.3	33	9.82	no defects
5	230	23.2	35	9.14	no defects
6	230	23.2	35	9.14	no defects
7	230	25.2	34	10.22	no defects

Table 6: Optimum weldability of 316Ti welded steel specimens at 15 mm thickness

Welding layer	Current (*I*)	Voltage (*V*)	Welding speed (cm/min)	Heat input (KJ/cm)	Presence of welding defects
1	190	27.3	19	16.38	no defects
2	190	26	38	7.8	no defects
3	190	26	38	7.8	no defects
4	190	26	38	7.8	no defects
5	190	26	38	7.8	no defects
6	190	26	38	7.8	no defects
7	190	26	38	7.8	no defects
8	190	26	38	7.8	no defects
9	190	26	38	7.8	no defects

Table 7: Optimum weldability of S355J2+N welded steel specimens at 15 mm thickness

Welding layer	Current (*I*)	Voltage (*V*)	Welding speed (cm/min)	Heat input (KJ/cm)	Presence of welding defects
1	195	25.9	17	17.38	no defects
2	230	28.6	38	10.38	no defects
3	230	26	32	11.21	no defects
4	230	26	32	11.21	no defects
5	230	26.8	35	10.56	no defects
6	230	27	35	10.64	no defects
7	232	26.9	34	11.01	no defects

After the integration of sufficient welding experiments with three different steels, it is obvious from the tables 5, 6 and 7 that there is a direct relationship between the heat input and the number of the welding defects. The results from the welding experiments demonstrated that both low and high heat input values increased the number and severity of welding defects. With

low heat input values, insufficient heat was applied to the workpieces, and incomplete fusion and lack of penetration were appeared. This resulted in defects such as porosity and cracks, as the weld metal solidifies too quickly, trapping gases or failing to adequately bond to the base material. Excessive heat input also increased the presence of cracking, undercutting, overlapping, spatter, and excessive weld bead size. Increased heat input also results in spatter, where droplets of molten metal are ejected from the weld pool, creating a messy surface and requiring additional post-weld cleaning. Additionally, high heat input created an overly large weld bead, which resulted in some cases in poor bead profiles, undercutting, and distortion. These findings highlight the importance of maintaining an optimum heat input values during welding to minimize defects and ensure the integrity of the welded joint.

The lower the heat input is applied during the welding execution, the lower the likelihood of appearance of welded defects. In HY 100 steel welded specimens and in S355J2+N steel welded specimens each welding layer must have different values of parameters such that the optimum weld quality is provided. Also it is worth mentioning that the values of the welding parameters which were applied in the welding layer 1 (or root layer) differ from the values of the welding parameters which were applied in the subsequent welding layers because it is desirable in the root layer to achieve high penetration and uniform weld bead by using lower values of welding speed and not so high values of current and voltage in order to maintain the heat input constant. The values of the welding current in the welding layers of HY 100 and S355J2+N steel welded specimens are higher than the relative values of the 316Ti steel welded specimens.

Macroscopic examination of the steel welded specimens with the optimum weldability

The macroscopic examination illustrated the distinguished regions of the welding layers and the regions of the HAZ, the parent metal and the filler metal of the steels under examination (see Figures 8, 9, 10). A scrutinized examination of each macro photograph identified some shadow regions with different darkness or brightness in the HAZ regions of the parent metal and these regions were created due to the complicated influence between each subsequent welding layer and the previous one.

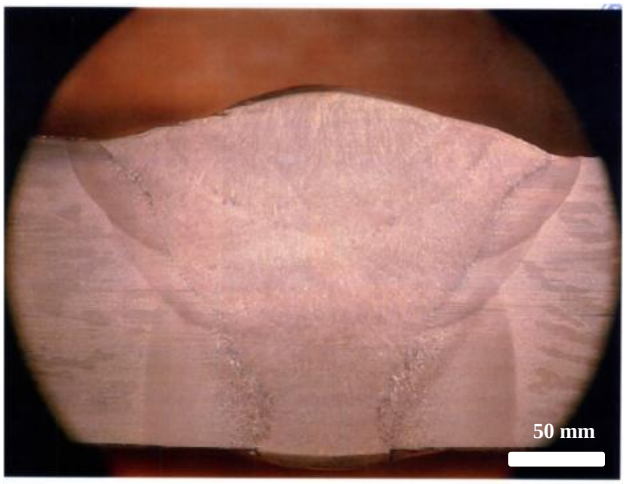

Figure 8: Macroscopic examination of HY 100 welded steel specimen.

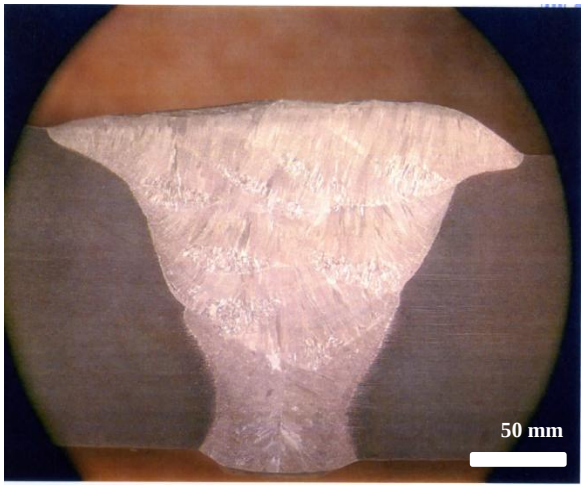

Figure 9: Macroscopic examination of 316Ti welded steel specimen.

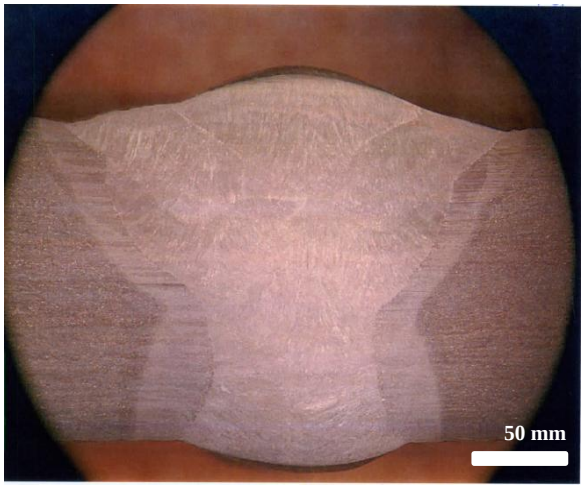

Figure 10: Macroscopic examination of S355J2+N welded steel specimen

Microscopic examination of the steel welded specimens with the optimum weldability

The microscopic examination illustrated the distinguished phases and the regions of the HAZ, the parent metal and the filler metal of the steels under examination (see Figures 12, 13, 14). The phases which were microscopically observed in the heat affected zone of the parent metal depend on the cooling rate of the austenite which is familiar from the iron – iron carbide phase diagram (Callister and Rethwisch, 2013).

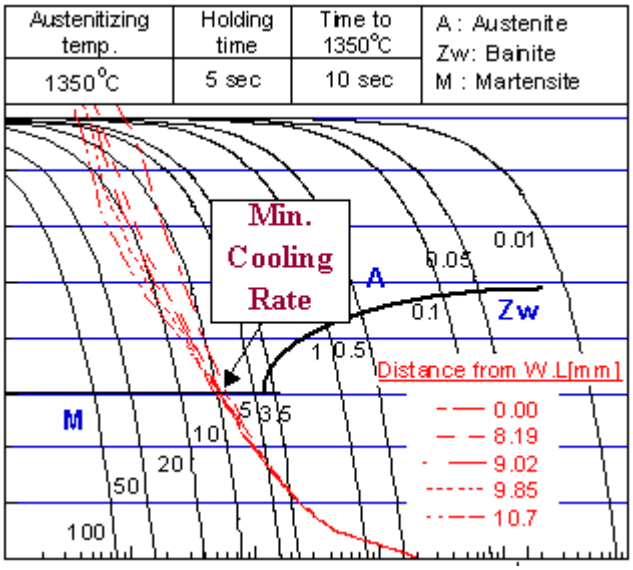

Figure 11: Schematic illustration of continuous cooling transformation (CCT) diagram for HY100 steel (Lee H.T. et al, 2007)

To support the interpretation of the weld and HAZ microstructures, the Continuous Cooling Transformation (CCT) diagram for the HY100 steel used in this study is shown in Figure 11. This diagram illustrates the transformation behavior of steel during cooling from an austenitizing temperature of 1350°C. It characterizes how the microstructure evolves as the material cools at varying rates, indicating the formation of different phases such as austenite (A), bainite (Zw), and martensite (M). The diagram shows that a specific minimum cooling rate is required to achieve each phase, with martensite forming at the highest cooling rates, followed by bainite at moderate rates. The cooling curves also highlight the time required to reach 1350°C and the corresponding transformation temperatures, providing critical insight into the steel's microstructural evolution. The "Min. Cooling Rate" curve specifically denotes the required cooling rates to achieve distinct phases, which is essential for understanding how cooling history influences the final microstructure. This CCT diagram is a valuable tool in

correlating cooling rates to phase transformations, offering key support for the microstructural analysis presented in this study.

Figure 12: Bainitic phase in the HAZ region of HY 100 welded steel specimen.

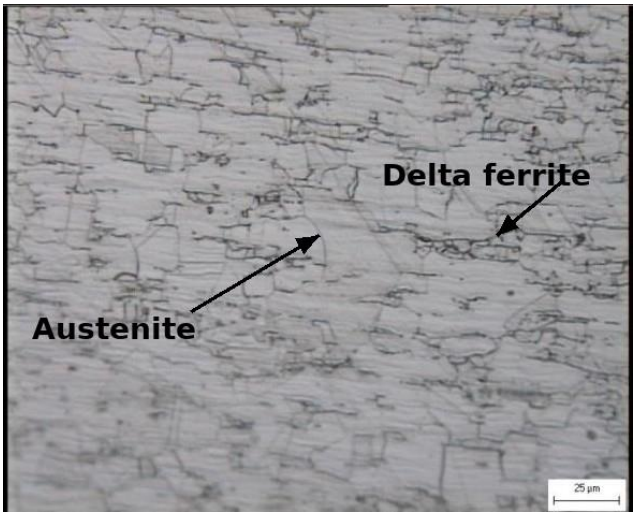

Figure 13: Austenitic and delta ferritic phase in the HAZ region of 316Ti welded steel specimen.

Figure 13 presents the microstructure in the HAZ of the 316Ti weld, where a mixture of austenite and delta ferrite is observed. The light, continuous matrix corresponds to austenite (shown in figure 13), while the darker, skeletal or vermicular networks are delta-ferrite. These phases form because, during welding, this region is heated well above the Ac_3 temperature into the fully austenitic field, but the high Cr and Mo contents of 316Ti shift the phase balance so that a fraction of liquid/solid transforms to delta ferrite on solidification. On subsequent cooling to room temperature, most of the structure transforms to austenite, whereas some delta-ferrite is retained as a stable phase, giving the two-phase austenite and delta microstructure seen in the HAZ.

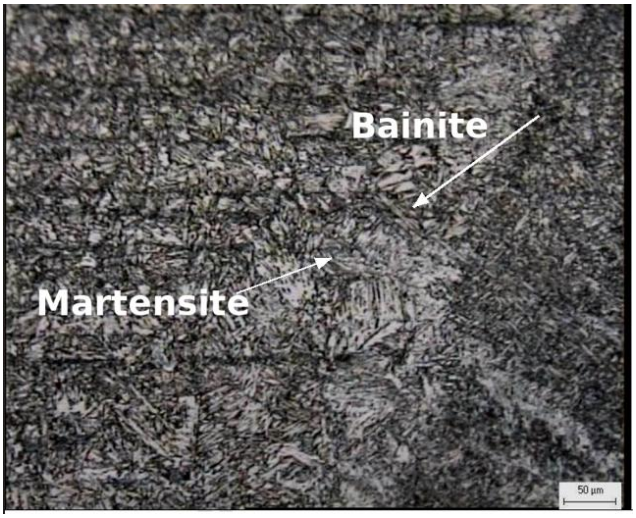

Figure 1: Bainitic and martensitic phase in the HAZ region of HY 100 welded steel specimen.

Figure 14 shows the heat-affected zone (HAZ) microstructure of the HY100 welded steel, consisting mainly of lath martensite and bainite. During welding, this region is heated into the fully austenitic field; on cooling, the high hardenability of HY100 (due to its Ni, Cr and Mo additions) shifts the CCT curves to longer times, so that the cooling path bypasses the ferrite–pearlite region and instead intersects the bainite and martensite transformation fields. Areas that cool very rapidly transform predominantly to untempered lath martensite, while regions experiencing slightly slower cooling form bainite or mixed martensite–bainite aggregates. This explains the predominance of fine acicular constituents and the absence of equilibrium phases in the HAZ.

For 10 mm thickness in HY100 steels the optimum welding conditions resulted in four (4) welding layers with welding current values at 170A, welding voltage values at 26Volt and heat input 10.02 KJ/mm.

For 10 mm thickness in 316Ti steels the optimum welding conditions resulted in four (4) welding layers with welding current values at 183A, welding voltage values at 27Volt and heat input 12.00 KJ/mm.

For 10 mm thickness in S355J2+N steels the optimum welding conditions resulted in four (4) welding layers with welding current values at 190A, welding voltage values at 26Volt and heat input 10.15 KJ/mm.

Determination of the corrosion resistance of the welded steels used in underwater marine systems

The presentation and discussion of the results which came from the experimental investigation of the corrosion resistance of the three steel specimens welded with the optimum welding parameters is included in this chapter.

Calculation of mass loss each welded steel specimen

The mass measurements of each welded steel specimen after 24, 48, 72, 96, 168, 192, 216, 240, and 264 hours of controlled corrosive environment exposure are presented in Table 2. After completing the Salt Spray Test, the mass loss of each welded specimen, calculated in accordance with the requirements of the specification ASTM G1-03 (2017), is presented in Table 8. The negligible increase in the mass of the 316Ti welded steel specimens is attributed to the entrapment of corrosion products within the exfoliated regions, which remained despite the cleaning process undertaken (ASTM G1-03, 2017).

Table 8: Mass measurements of each welded steel specimen

Exposure period (hours)	HY 100 welded steel specimen (gr)	S355J2+N welded steel specimen (gr)	316Ti welded steel specimen (gr)
0	7298	6281	7555
24	7301	6284	7556
48	7303	6287	7556
72	7305	6290	7557
96	7310	6305	7556
168	7313	6307	7557
192	7318	6309	7557
216	7319	6314	7557
240	7322	6318	7557
264	7326	6320	7557
After 300 hours exposure and removal of corrosion products	7264	6218	7556

Table 9: Mass loss of each welded specimen after the integration of the Salt Spray Test

Mass loss	HY 100 welded steel specimen (gr)	S355J2+N welded steel specimen (gr)	316Ti welded steel specimen (gr)
Initial mass before exposure (W_1)	7298	6281	7555
Mass after 300 hours exposure and removal of corrosion products (W_2)	7264	6218	7556
Mass loss (W1 – W2)	34	63	negligible

The mass measurements of each welded steel specimen without removing the salt deposits at specific periods of exposure is illustrated below (see Figures 15, 16, 17).

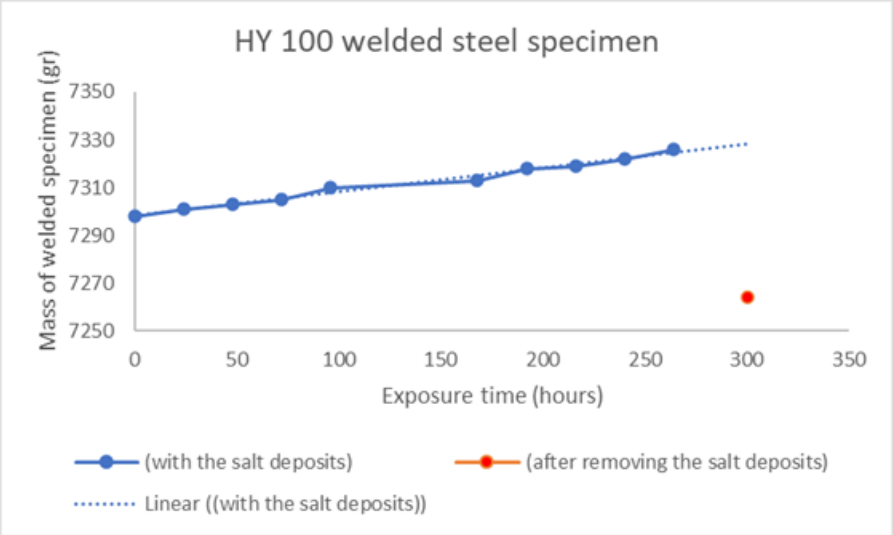

Figure 15: Mass measurements of HY 100 welded steel specimen at specific periods of exposure

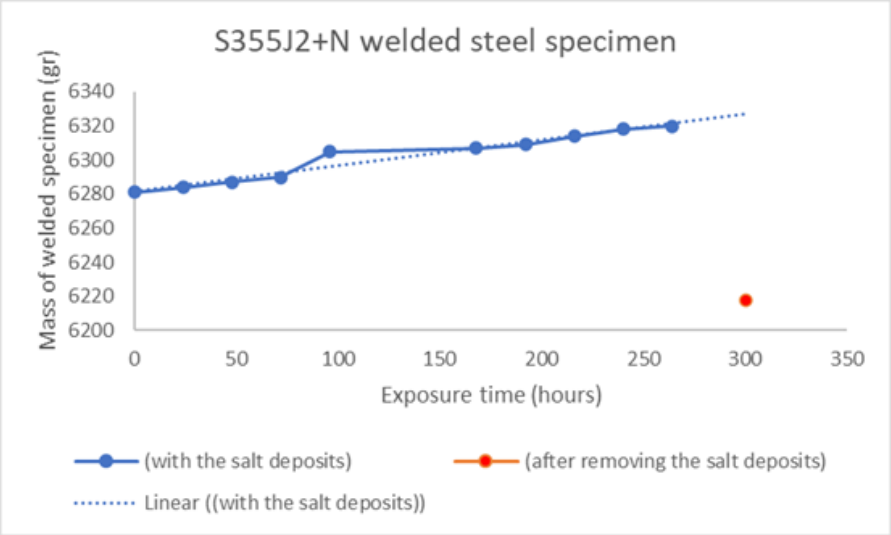

Figure 16: Mass measurements of S355J2+N welded steel specimen at specific periods of exposure

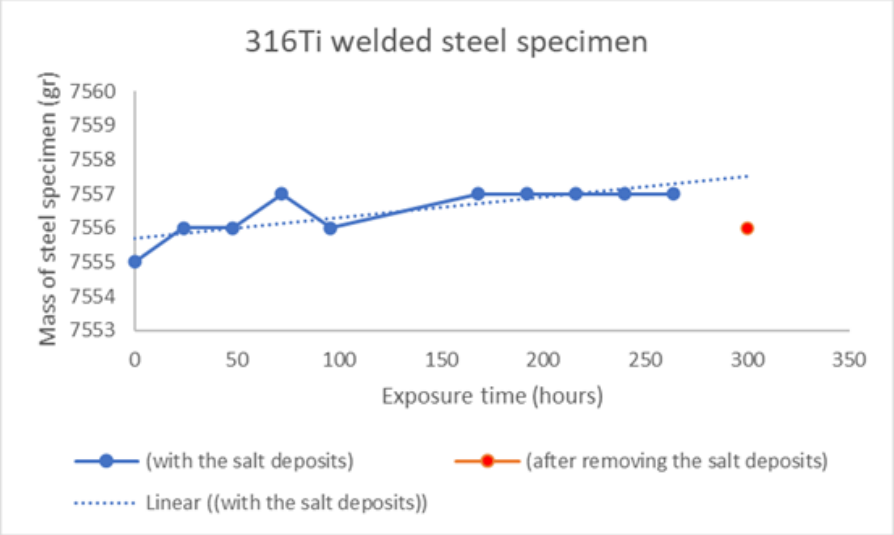

Figure 17: Mass measurements of 316Ti welded steel specimen at specific periods of exposure

After the integration of the Salt Spray Test, it is evident from Table 9 and Figures 15, 16, and 17 that there is a relationship between the mass values and the period of exposure for each welded specimen. The 316Ti welded steel specimen did not present any significant mass loss due to its chemical composition, which provides exceptionally high resistance to corrosion and oxidation (American Welding Society [AWS], 1998).

Microscopic examination of the surfaces of the welded specimens after the integration of Salt Spray Test

Microscopic examination of each welded steel specimen under examination was executed with the aid of optical microscope and Scanning Electron Microscope (SEM) for the assessment of the corrosion morphology after the calculation of the relative mass loses and the relative outputs are presented for each case:

- The HY 100 welded steel specimen illustrated pitting corrosion (see Fig. 18). The maximum pit depth was measured 40 – 50 μm observed in the weld zone. SEM/EDS analysis was conducted within the pits and representative results are depicted in Fig. 19 and table 10. This analysis indicated that the corrosion products are oxides, while some Cl remained despite the cleaning process executed after the integration of the Salt Spray Test.

- The S355J2+N welded steel specimen exhibited pitting corrosion (see Fig. 20). The pitting corrosion is characterized by deeper pits up to 100 μm. The deeper pits were located at the weld metal.

- The X6CrNiMo17-12-2 (316Ti) austenitic stainless welded steel specimen is characterized by exfoliation corrosion on the weld metal (see Fig. 21). The penetration depth of the corrosion is approximately 25 μm. Corrosion front evolves preferentially via the ferrite phase. SEM/EDS analysis was carried out at selected areas, with corrosion evidence. Typical results are depicted in Fig. 22 and table 11. The corrosion products are oxides, while significant presence of Cl was detected even after the cleaning process performed after the completion of the Salt Spray Test.

The low mass losses for all specimens under investigation, is attributed to the welding process employed for their manufacturing (robotic FCAW).

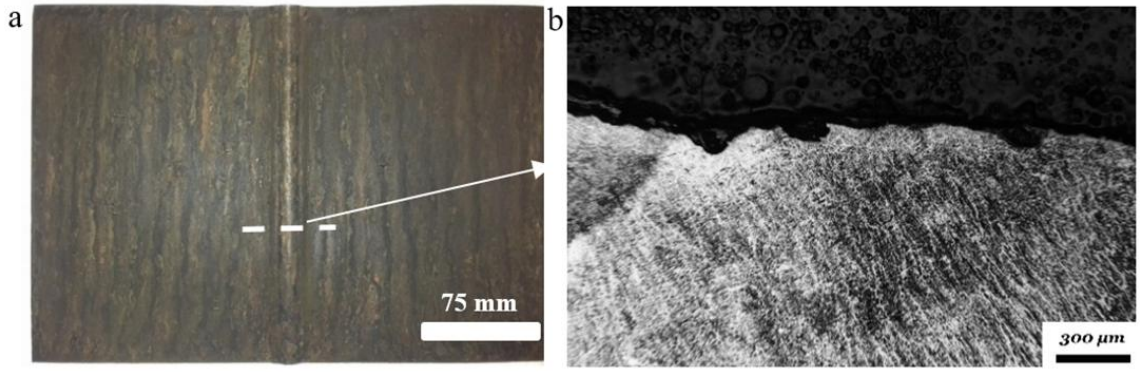

Figure 18: HY 100: (a) Specimen surface after salt spray test. Dash line indicates the area of the metallographic examination on transverse cross section; (b) Morphology of pitting corrosion at the weld metal

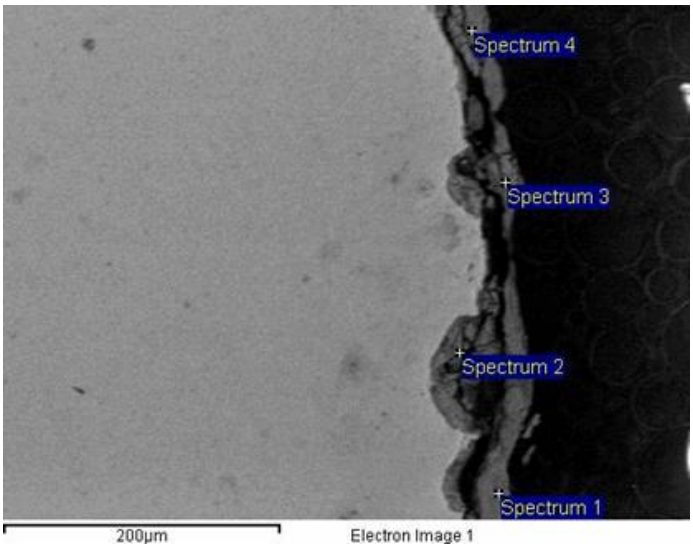

Figure 19: HY 100: SEM image at the corroded area, located at the face of the weld metal.

Table 10 HY 100: EDS semi-quantitative analysis of the corrosion products accumulated within the pits (wt %)

Spectrum (see fig.19)	O	Mg	Si	Cl	Cr	Fe	Mo
Spectrum 1	50.27	---	---	2.71	---	47.02	---
Spectrum 2	44.86	---	1.20	---	---	53.94	---
Spectrum 3	51.63	---	0.37	0.19	0.71	47.09	---
Spectrum 4	50.61	0.26	---	0.74	0.49	47.25	0.65

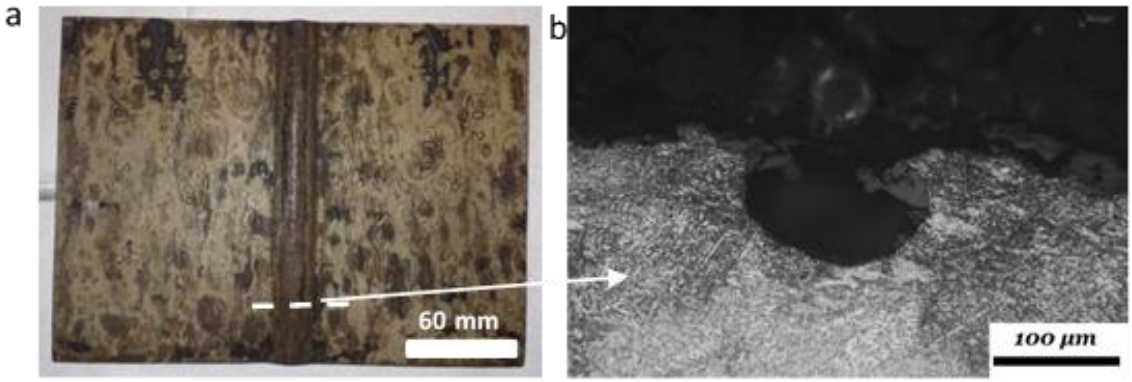

Figure 20 S355J2+N: (a) Specimen surface after salt spray test. Dash line indicates the area of the metallographic examination on transverse cross section; (b) Morphology of pitting corrosion at the weld metal

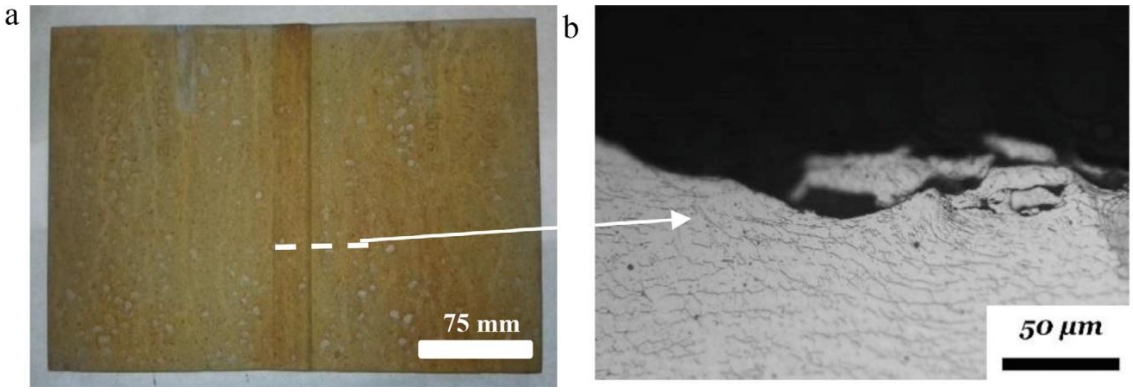

Figure 21 316Ti: (a) Specimen surface after salt spray test. Dash line indicates the area of the metallographic examination on transverse cross section; (b) Morphology of exfoliation corrosion at the weld metal

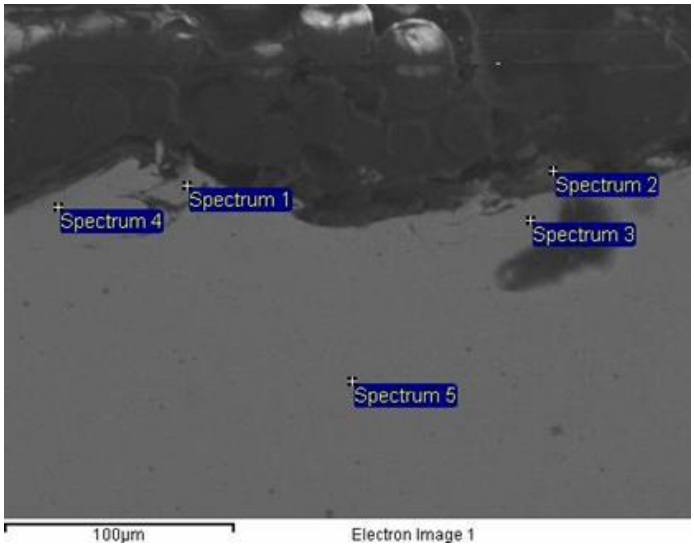

Figure 22 316Ti: SEM image of the corroded area located at the face of the weld metal.

Table 11 316Ti: EDS semi-quantitative analysis of the corrosion products accumulated within the pits (wt %)

Spectrum (see fig. 23)	O	Si	Cl	Cr	Fe	Ni	Mo
Spectrum 1	---	0.88	---	20.82	64.30	9.55	4.44
Spectrum 2	64.05	---	12.89	5.83	17.24	---	---
Spectrum 3	---	1.39	---	20.95	64.51	10.25	2.90
Spectrum 4	---	0.92	---	18.76	64.81	12.53	2.98
Spectrum 5	---	1.45	---	22.19	61.85	12.60	1.91

Determination of corrosion resistance of the welded steel specimens under examination

The corrosion rate of the welded steel specimens under examination was determined by the following equation (ASTM G1, 2017)

$$\text{Corrosion Rate} = \frac{\text{K} \cdot \text{W (g)}}{\text{A (cm2)} \cdot \text{T(hours)} \cdot \text{D}(\frac{\text{g}}{\text{cm3}})}$$

Where:

K = a constant

T = time of exposure in hours

A = area in cm^2

W = mass loss in grams, and

D = density in g/cm^3

Table 12 illustrates the values of the corrosion rates of the HY100 welded steel specimen and the S355J2+N welded steel specimen. The HY 100 welded steel specimen illustrated higher corrosion resistance than the S355J2+N welded steel specimen.

Table 12 Corrosion rate of each welded specimen after the integration of the Salt Spray Test

Welded steel specimen	Corrosion rate (mm/year)
HY 100 welded steel specimen	0.884
S355J2+N welded steel specimen	1.949

Fatigue Performance and Corrosion Resistance of Welded Steels

The fatigue performance and corrosion resistance of welded steel specimens were evaluated to understand their suitability for applications in marine and structural environments. Three materials, HY100, S355J2+N, and 316Ti, were tested under cyclic loading and tensile stress to analyze their behavior in both corroded and non-corroded conditions. These materials were chosen for their unique mechanical properties and ability to withstand environmental stresses. The experiments followed ASTM E466 for fatigue testing and ASTM E8 for tensile testing, providing consistent and reliable datasets.

The tests were performed using an MTS 322 servo-hydraulic machine with a maximum capacity of 250 kN. For fatigue tests, cyclic loading parameters were defined as percentages of the materials' yield strength, with a stress ratio (R) of 0.1 and a frequency of 10 Hz. Corrosion resistance was evaluated through pre-exposure to saline environments, and tensile properties were tested to determine yield strength, tensile strength, and elongation.

Tensile Properties

The tensile test results which are needed as a precondition of fatigue tests, presented in Tables 13, 15, 17, demonstrate the mechanical robustness of the three materials. HY100 exhibited the highest tensile strength, ranging from 700 to 750 MPa, and an ultimate tensile strength of 861 MPa. Its elongation ranged from 18% to 20%, reflecting a good balance between strength and ductility. In comparison, 316Ti showed lower tensile strength (339–348 MPa) but significantly higher elongation at 35.1%, indicating superior ductility. S355J2+N achieved moderate values, with tensile strength between 574 and 580 MPa and elongation ranging from 16.7% to 20.2%. These results highlight the varying mechanical characteristics of the materials: HY100 for strength-critical applications, 316Ti for ductility in corrosive environments, and S355J2+N for cost-effective structural use. The stress-strain diagram provided in Figure 23 further illustrates these differences.

Table 13: HY 100 tensile test result

Spec. No	Yield Strength [MPa]	Tensile Strength [MPa]	Elongation (%)
1	700	861	20
2	750	861	18

Table 14: HY100 fatigue test results

	σ_{max} [MPa]	σ_{min} [MPa]	cycles to failure, N_f
Non corroded	560	56	40.377
			21.057
	420	42	43.272
			82.665
	280	28	234.101
			303.239
	230	23	3.284.300
Corroded	560	56	17.991
			21.308
	420	42	46.653
			57.145
	280	28	217.915
			293.399
	230	23	2.593.500

Table 15: S355 J2+N tensile test results

Spec. No	Yield Strength [MPa]	Tensile Strength [MPa]	Elongation (%)
1	430	574	16,7
2	441	580	20,2

Table 16: S355 J2+N tensile test results

	σ_{max} [MPa]	σ_{min} [MPa]	cycles to failure, N_f
Non corroded	349	34,9	360.703
	262	26,2	4.343.257 (run out)
	175	17,5	-
Corroded	349	34,9	296.175
	262	26,2	2.539.189 (no failure)
	175	17,5	1.655.386 (no failure)

Table 17: 316Ti tensile test results

Spec. No	Yield Strength [MPa]	Tensile Strength [MPa]	Elongation (%)
1	339	603	35,1
2	348	603	35,1

Table 18: 316Ti fatigue test results

	σ_{max} [MPa]	σ_{min} [MPa]	cycles to failure, N_f
Non corroded	343,5	34,35	37.931
	275	27,5	449.505
	206	20,6	2.867.696 (No failure)
	137	13,7	3.478.268 (No failure)
Corroded	275	27,5	115.011
	206	20,6	475.498
	137	13,7	3.227.630 (No Failure)

Fatigue Performance

Fatigue tests revealed significant differences in performance between corroded and non-corroded specimens, with each material responding uniquely to environmental and mechanical stress. The detailed results are summarized in Tables 14, 16, and 18.

HY100 demonstrated exceptional fatigue life under non-corroded conditions, achieving over 10 million cycles without failure at 20% of its yield strength. However, when exposed to corrosion, its performance dropped markedly. For instance, at 30% of its yield strength, the number of cycles to failure reduced to 2.593.500 highlighting the material's susceptibility to corrosion.

S355J2+N, under non-corroded conditions, achieved a fatigue life of up to 4.3 million cycles at 60% of its yield strength. However, similar to HY100, its performance declined significantly in corrosive environments. At the same stress level, the fatigue life dropped to approximately 2.5 million cycles, showing moderate resistance to corrosion compared to HY100.

316Ti maintained robust performance even under corroded conditions. Non-corroded specimens achieved a fatigue life of 3.5 million cycles at 40% of yield strength, while corroded specimens exhibited only a slight reduction, with cycles to failure at approximately 3.2 million. This behavior underscores 316Ti's superior corrosion resistance, making it an ideal choice for marine environments.

The fatigue results, emphasize the significant impact of corrosion on fatigue life. HY100 excelled in high-stress scenarios but showed a dramatic decline in performance under corrosive conditions. In contrast, 316Ti demonstrated resilience, maintaining high fatigue life despite exposure to corrosive environments. S355J2+N offered a balanced performance, providing reasonable fatigue resistance at a lower cost.

Figure 23: stress-strain diagram for HY100, illustrating the material's mechanical behaviour during tensile testing. This figure typically shows how HY100 responds to applied stress.

The results underscore the importance of material selection based on environmental factors and stress requirements. For marine applications where corrosion is prevalent, 316Ti stands out as the optimal choice. HY100, with its superior tensile and fatigue strength, is best suited for high-stress environments with controlled corrosion. S355J2+N, with its moderate properties, offers a cost-effective solution for general structural applications.

Figure 24: Non-corroded (top) and corroded (bottom) specimens after the fatigue test.

Figure 25: Corroded and non-corroded samples for HY 100. X: indicates surfaces to be subjected in metallographic preparation (grinding, polishing, and etching).

Figure 26: Non-corroded and corroded samples for two materials. X: indicates surfaces to be subjected in metallographic preparation (grinding, polishing, and etching).

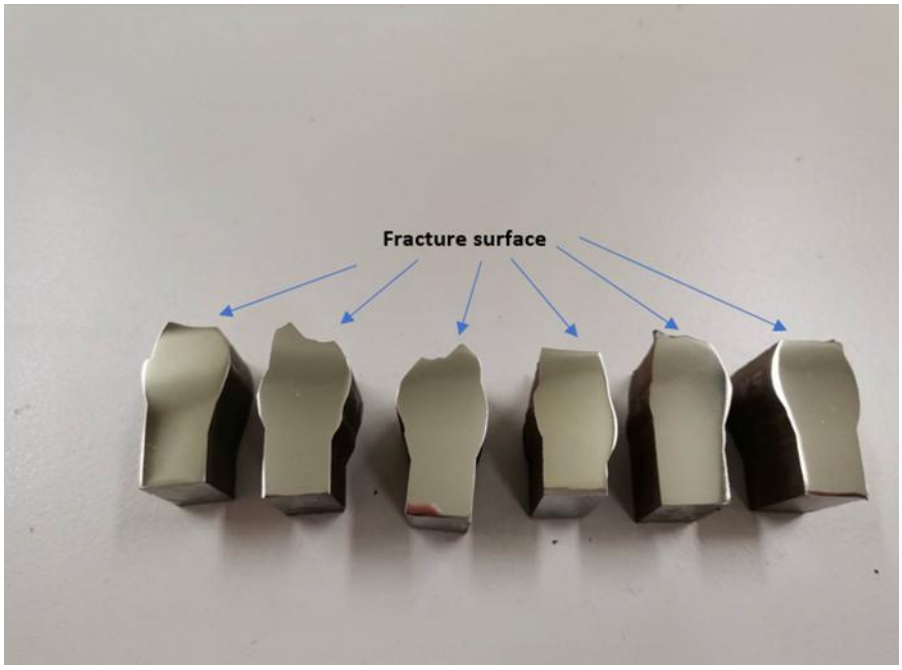

Figure 27: Fractured surfaces of the materials

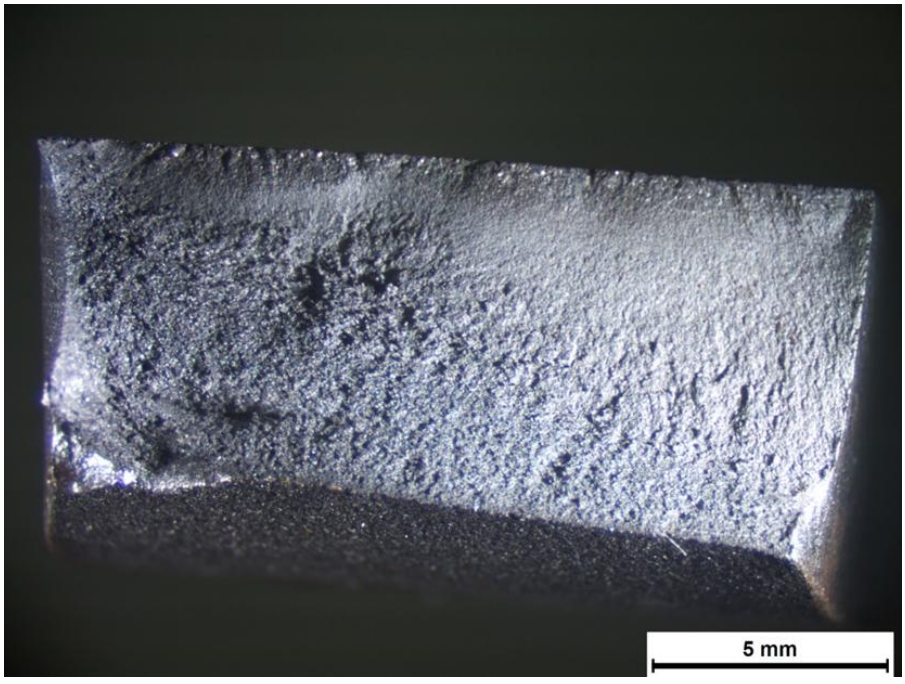

Figure 28: Fractured surface of S355J2+N uncorroded material

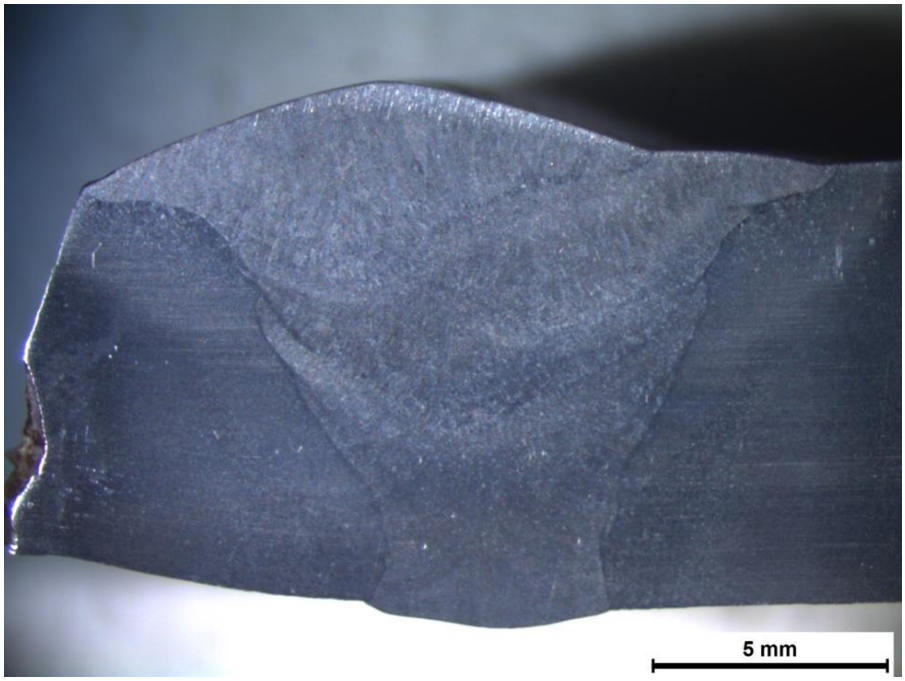

Figure 29: Macroscopic examination of S355J2+N uncorroded material

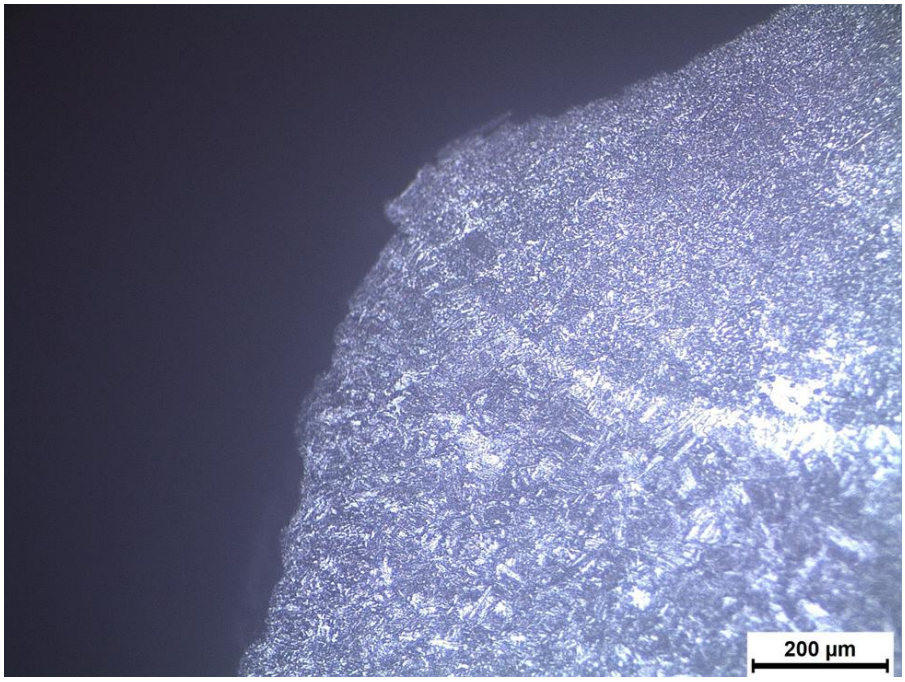

Figure 30: Microscopic examination of S355J2+N uncorroded material

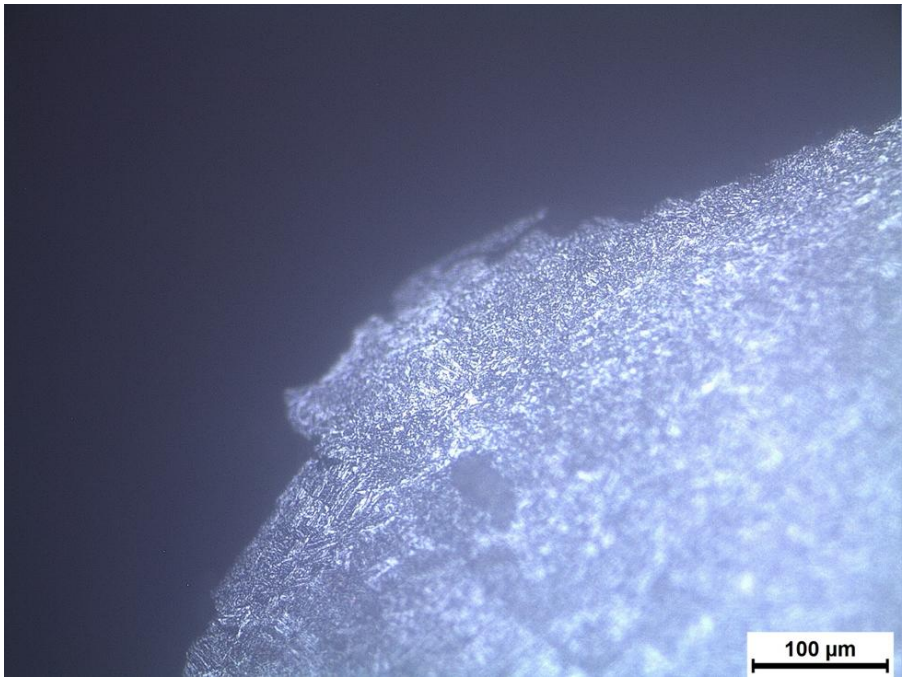

Figure 31: Microscopic examination of S355J2+N uncorroded material

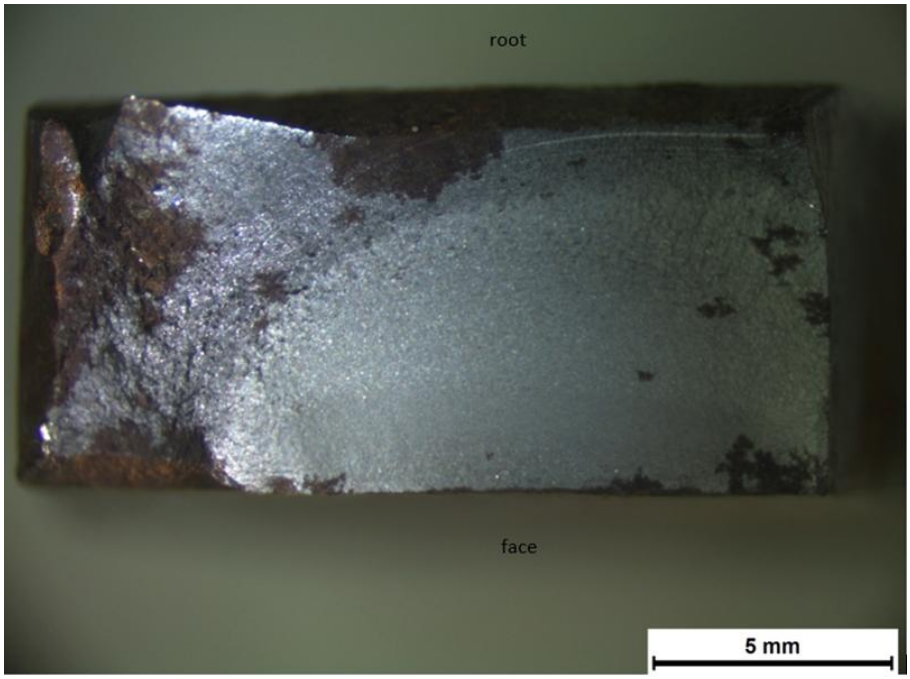

Figure 32: Corroded fracture surface of S355J2+N material

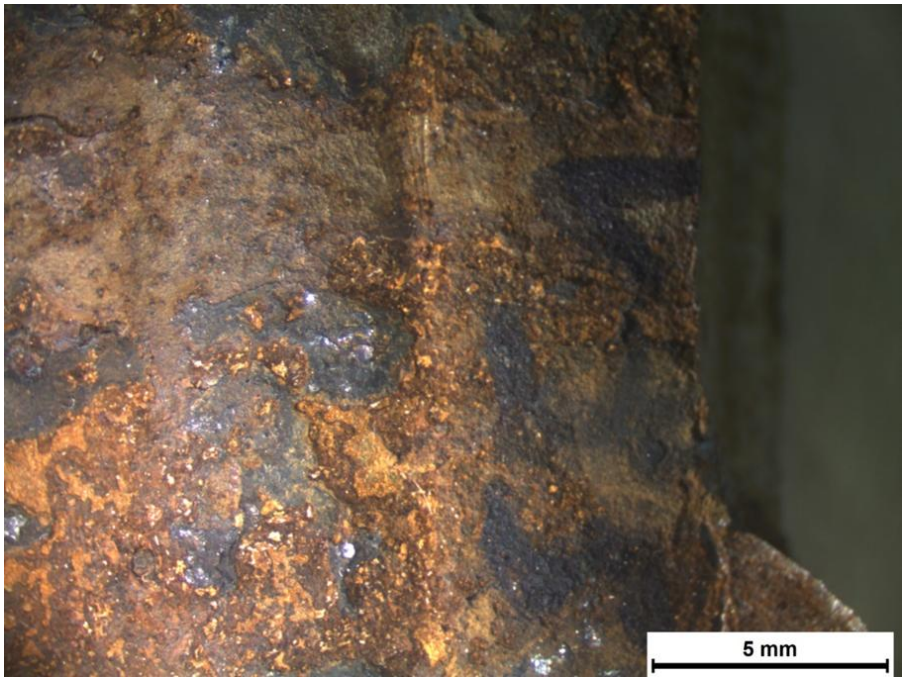

Figure 33: Corroded fracture surface of S355J2+N material

Figure 34: Corroded fracture surface of S355J2+N material

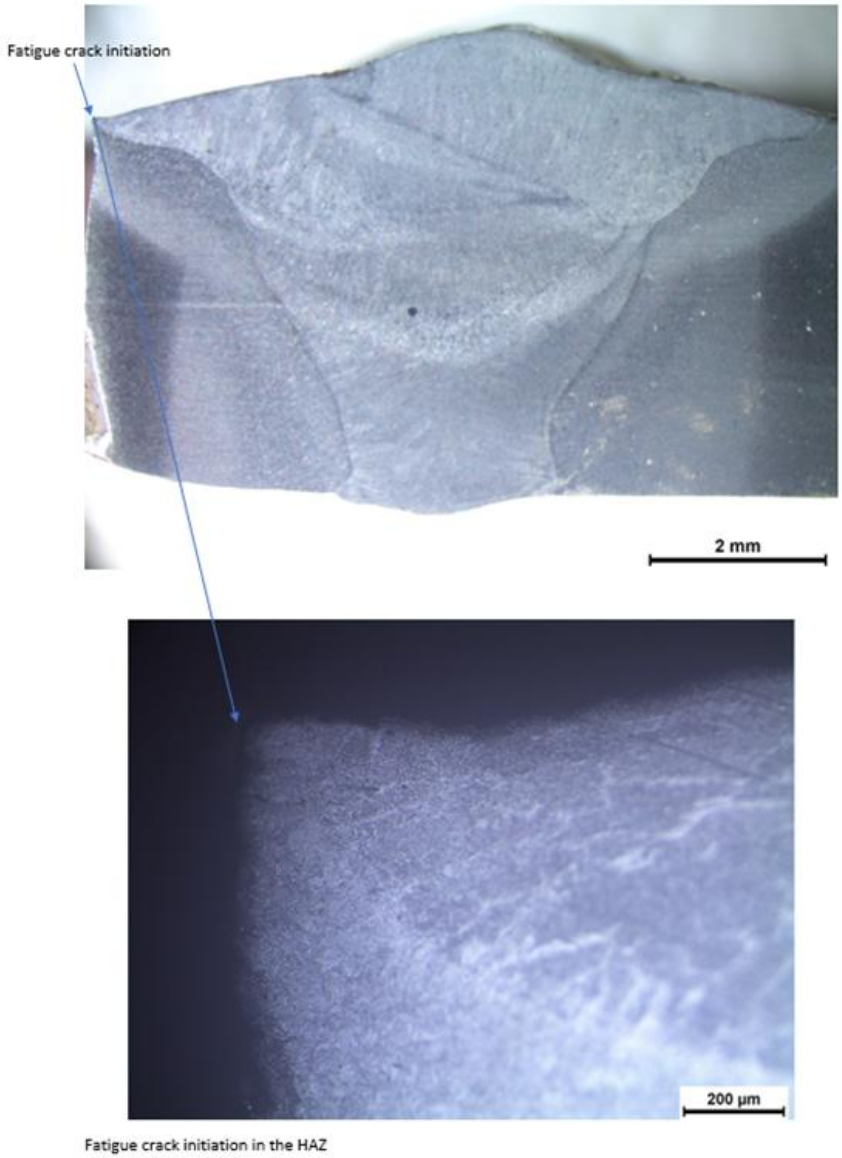

Figure 35: Fatigue crack initiation in HAZ of S355J2+N material

In Figure 35 the fatigue crack is clearly shown to initiate in the heat-affected zone (HAZ) adjacent to the weld toe, rather than in the weld metal or in the bulk parent material. The macro-fractograph (upper image) reveals a semi-elliptical fatigue region whose origin coincides with the intersection of the specimen surface and the HAZ, while the higher-magnification image (lower) indicates a slightly rough, micro-notched surface in this region. This location is mechanically and metallurgically critical: the weld toe geometry introduces a pronounced stress concentration under cyclic loading, and the adjacent HAZ contains steep gradients in microstructure and hardness arising from the welding thermal cycle. As a result, the local tensile stresses and plastic strain amplitudes at the toe/HAZ interface are significantly higher than in the surrounding material, promoting early crack nucleation at pre-existing micro-notches,

inclusions or slip bands. Once initiated, the crack propagates through the HAZ following the direction of maximum tensile stress, as evidenced by the curved fatigue crack front and the progressive change in fracture appearance away from the initiation site. The observation that fatigue consistently initiates in this region confirms that the weld toe/HAZ combination is the dominant fatigue-limiting feature of the joint, and underscores the importance of weld profile control, residual-stress management and microstructural optimisation in improving the fatigue performance of these welded specimens.

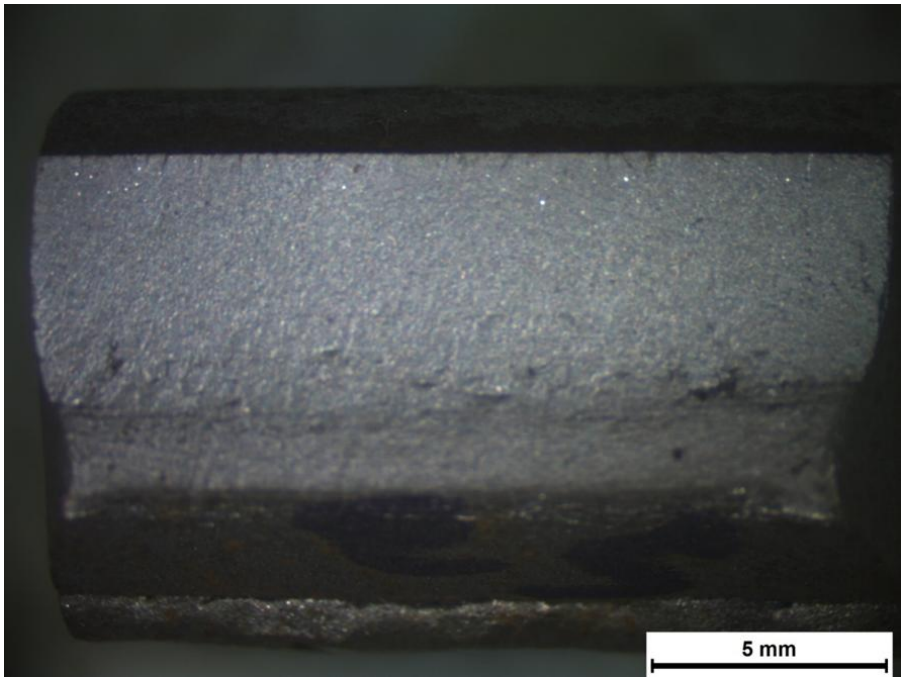

Figure 36 Fractured surface of 316Ti uncorroded material

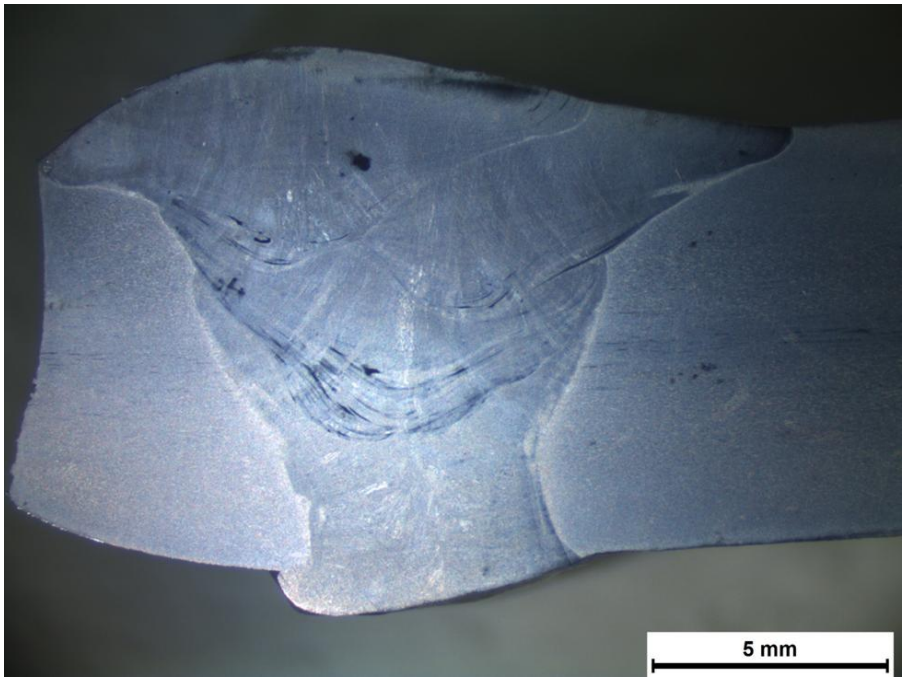

Figure 37: Macroscopic examination of fractured 316Ti uncorroded material

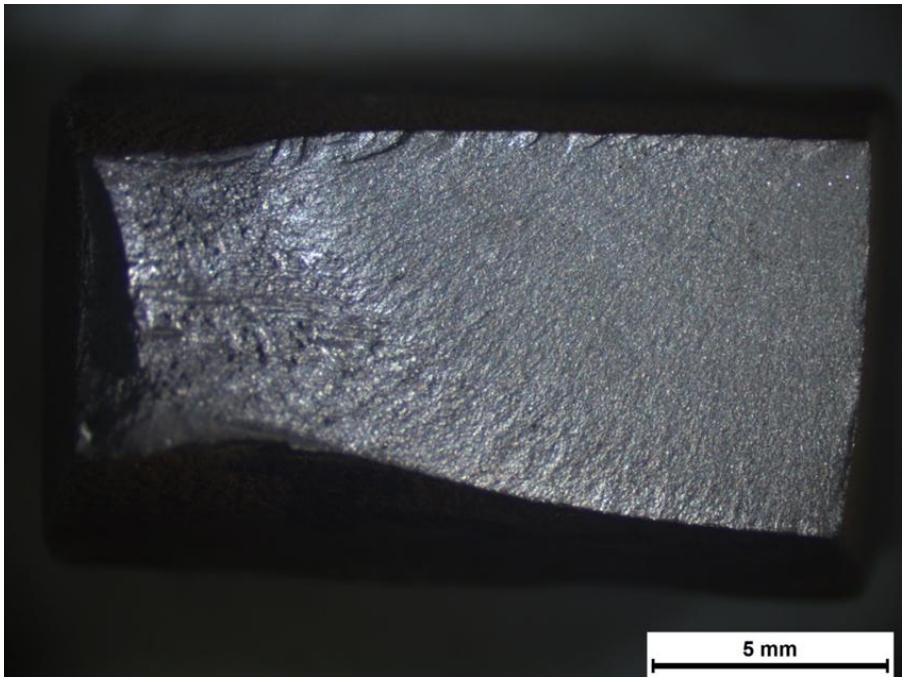

Figure 38: Fractured surface of 316Ti corroded material

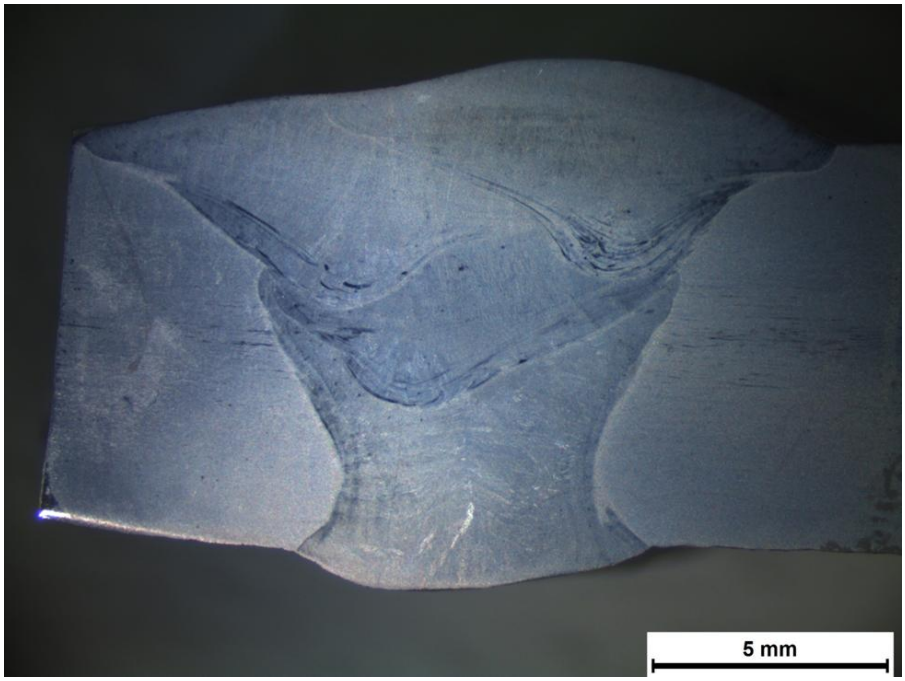

Figure 39: Macroscopic examination of fractured 316Ti uncorroded material

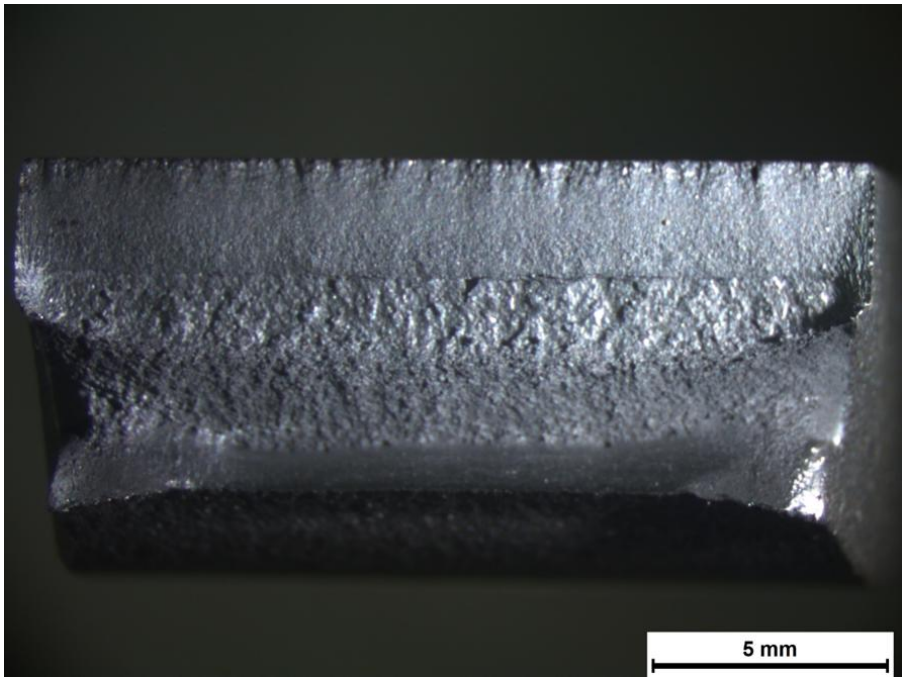

Figure 40: Fractured surface of HY100 uncorroded material

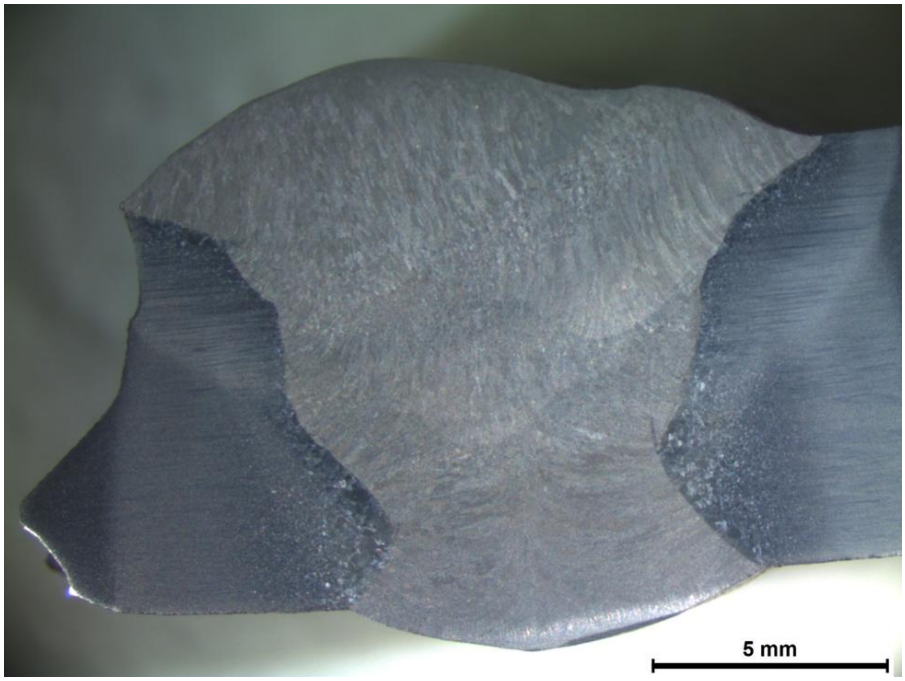

Figure 41: Macroscopic examination of HY100 uncorroded material

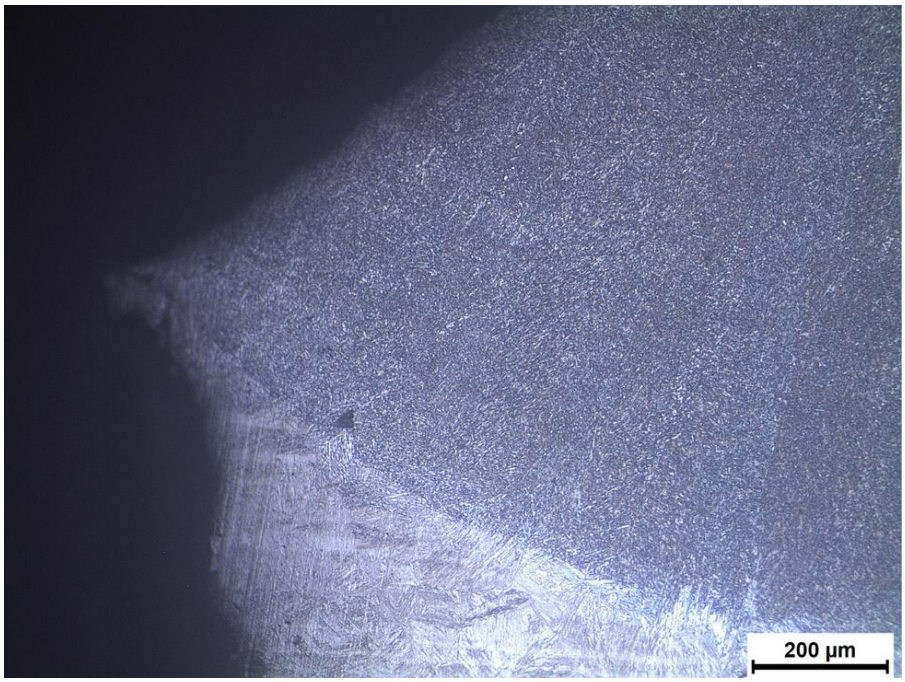

Figure 42: Microscopic examination of HY100 uncorroded material

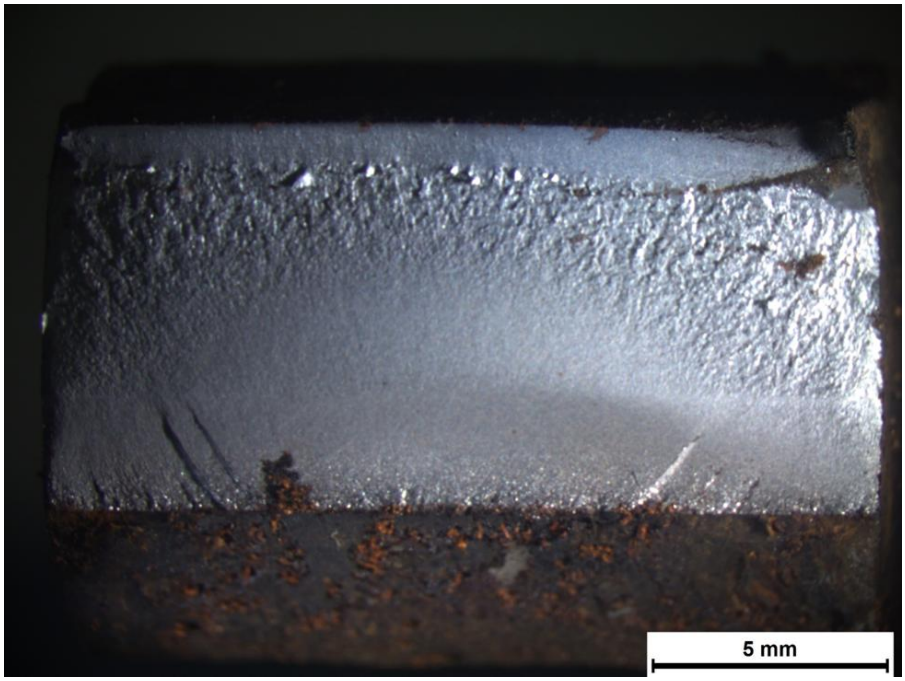

Figure 43: Fractured surface of HY100 corroded material

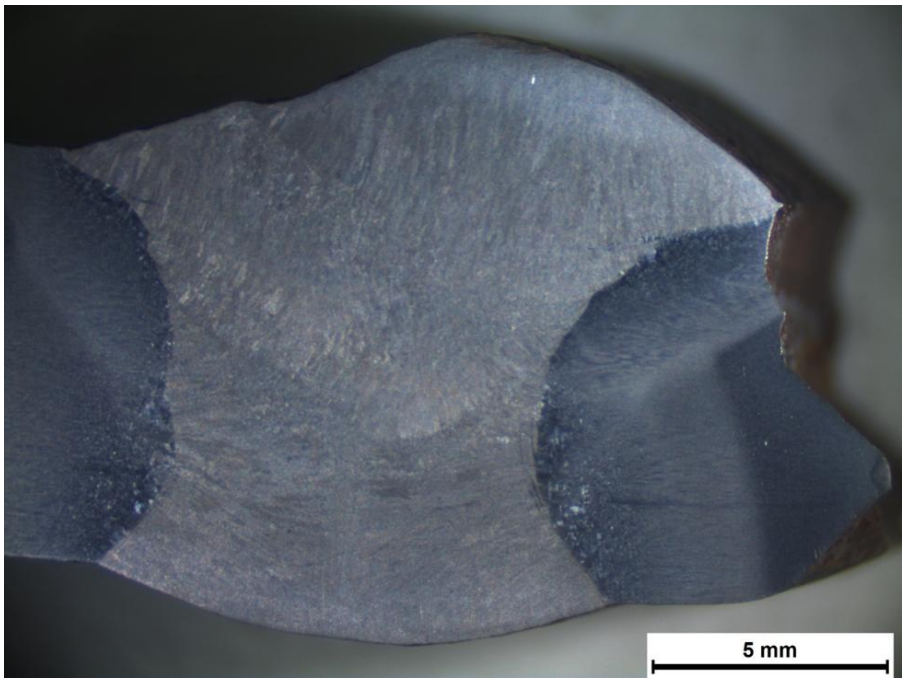

Figure 44: Macroscopic examination of HY100 corroded material

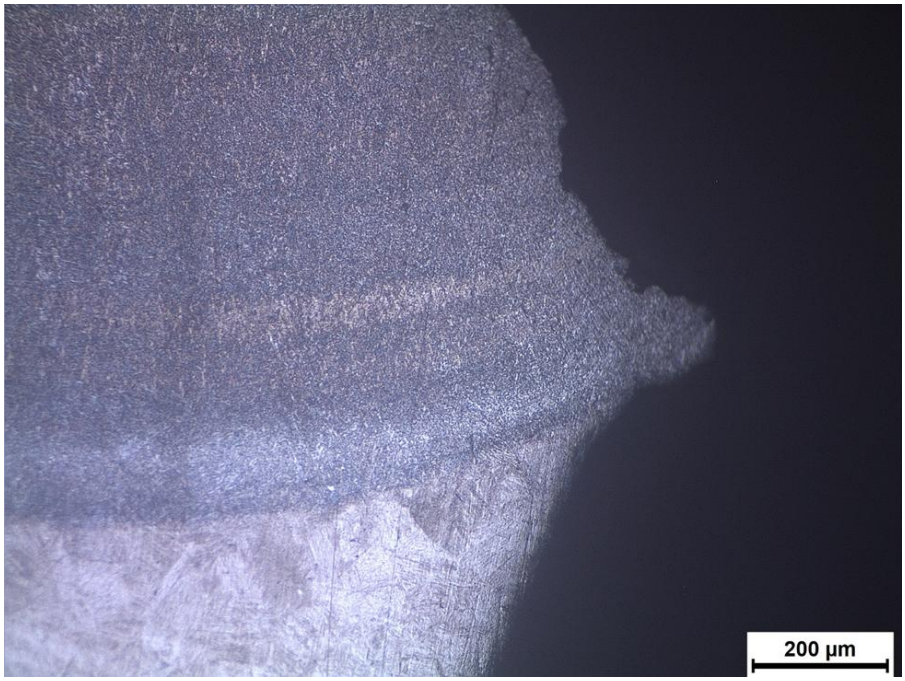

Figure 45: Microscopic examination of HY100 corroded material

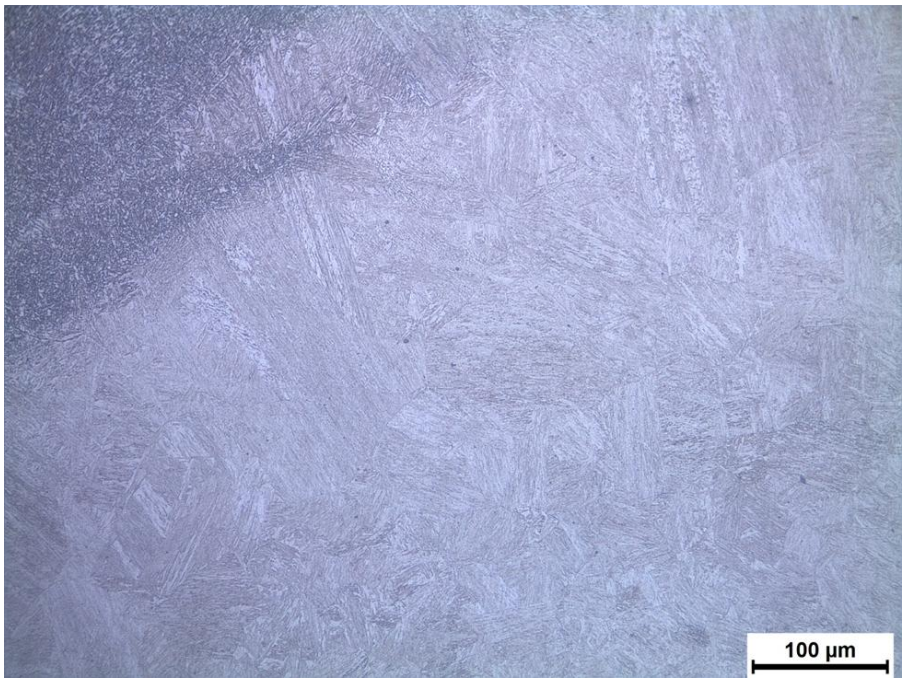

Figure 46: Microscopic examination of HY100 corroded material

S-N curves

The comparative analysis of HY 100, S355 J2+N, and 316 Ti highlights significant differences in their fatigue performance, mechanical properties, and resistance to environmental factors (Figures 47, 48, 49). HY 100 exhibits moderate fatigue performance in uncorroded conditions but there is a significant reduction in fatigue life when exposed to corrosive environments. This reduction underscores its sensitivity to environmental degradation, such as saltspray exposure, which accelerates fatigue crack initiation and propagation. While its performance aligns moderately with IIW standards, its susceptibility to corrosion implies that additional safety factors may be required in design considerations for critical applications.

S 355 J2+N, on the other hand, displays moderate-to-low fatigue limits, with a steeper reduction in fatigue life under corrosive conditions. This significant deterioration underlines the material's vulnerability to aggressive environments. While it shows good alignment with IIW standards in uncorroded states, its fatigue life diverges significantly when pre-corroded, suggesting that the standards may not adequately address environmental factors for this material. These findings highlight its limitations for high-cycle fatigue applications, particularly in offshore or marine environments where corrosion is prevalent.

In contrast, 316 Ti outperforms the other two materials, exhibiting higher fatigue resistance in both uncorroded and corroded conditions. The reduction in fatigue life for 316 Ti due to corrosion is comparatively less pronounced demonstrating its reliability in environments where corrosion is a major concern. Although it has not been explicitly tested against IIW standards, its performance in fatigue and corrosion environments suggests it is well-suited for applications where these factors are critical, such as in the marine and chemical industries.

From a mechanical properties perspective, HY 100 stands out with the highest yield strength (690 MPa) and tensile strength, making it ideal for high-stress environments. However, its fatigue life under corrosive conditions may limit its application in environments that experience both cyclic loading and corrosion. S 355 J2+N, with its lower yield strength of 355 MPa, is less robust for high-stress applications. Combined with its high susceptibility to corrosion-induced fatigue, its utility becomes more constrained in aggressive environments. Meanwhile, 316 Ti, despite having the lowest yield strength at 300 MPa, compensates for this with excellent corrosion resistance and relatively high fatigue limits. These attributes align well for applications where long-term exposure to harsh conditions is unavoidable.

The microstructural characteristics of these materials also play a crucial role in their fatigue and corrosion performance. HY 100, provides good mechanical strength but has limited corrosion resistance, contributing to its significant fatigue life reduction in corroded conditions. S355 J2+N, offers enhanced weldability but is more susceptible to corrosion-induced fatigue due to the influence of geometric imperfections and the presence of corrosion pits. In contrast, the austenitic stainless-steel structure of 316 Ti offers exceptional corrosion resistance. Its homogeneity minimizes the formation of corrosion pits, which are typical initiation points for fatigue cracks, thus enhancing its performance in cyclic loading conditions.

In terms of applications, HY 100 is best suited for industries such as shipbuilding and pressure vessels, where its high strength is advantageous. However, its performance in corrosive environments requires additional protective measures like coatings or controlled environments. S355 J2+N finds application in structural components with lower cyclic stresses and less corrosive settings. Its performance in offshore and marine applications would require close monitoring and potential enhancement. Conversely, 316 Ti is the material of choice for marine and chemical industries, where it demonstrates exceptional reliability and resistance to environmental degradation.

The analysis also points to the need for revisiting fatigue design standards, such as those provided by IIW. While the standards provide a reasonable estimate for the fatigue behavior of HY 100 and S355 J2+N in non-corrosive conditions, they may fail to account for the pronounced effects of corrosion. The superior performance of 316 Ti further suggests the necessity of incorporating material-specific responses under environmental degradation into these standards to improve their predictive accuracy.

In conclusion, the selection of materials for fatigue-critical applications must strike a balance between mechanical properties, fatigue resistance, and corrosion behavior. HY 100 and S 355 J2+N are suitable for non-corrosive settings but may require additional measures for durability in aggressive environments. 316 Ti, with its consistent performance under fatigue and corrosion, emerges as a reliable choice for harsh environmental conditions. Future work should aim to refine standards and explore post-weld treatments to enhance the fatigue resistance of these materials, particularly in challenging environments.

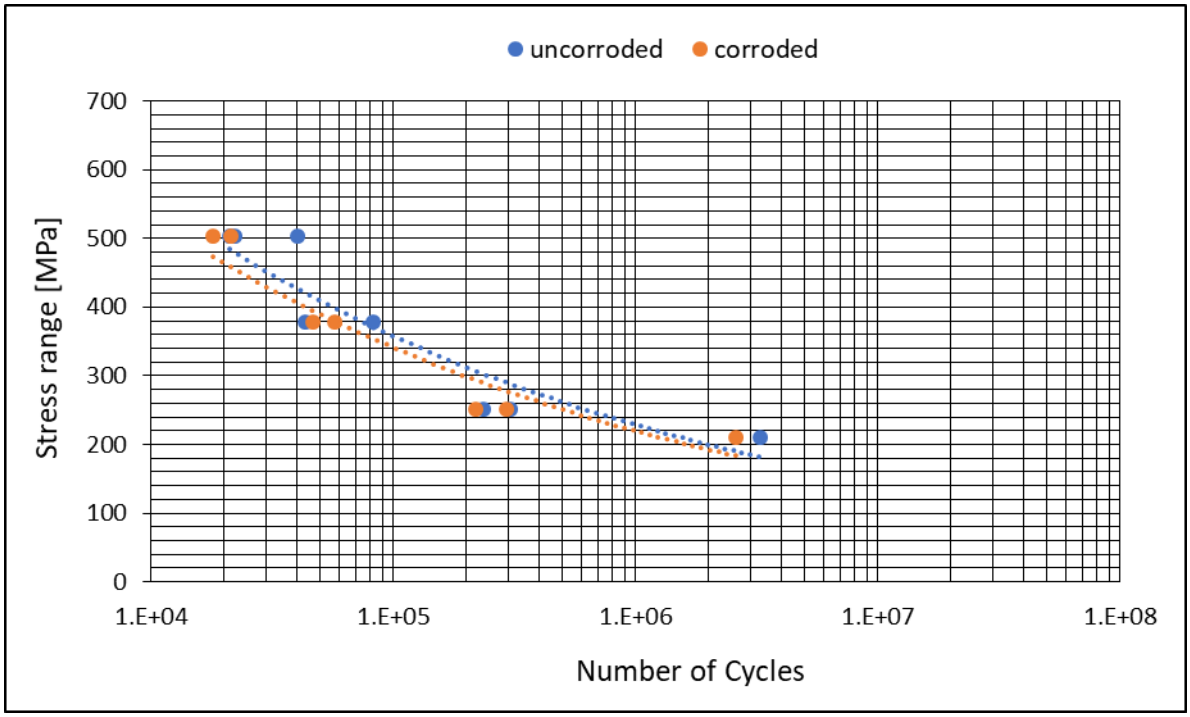

Figure 47: Experimental fatigue results for HY 100 butt welds (uncorroded and corroded samples).

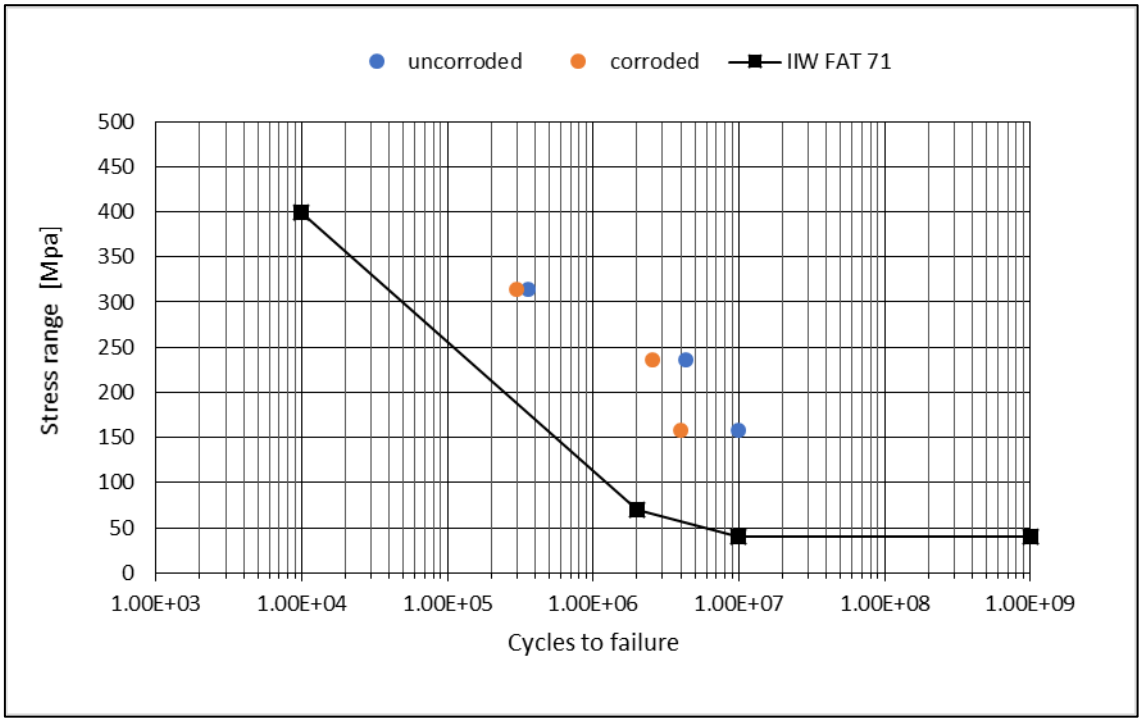

Figure 48: Experimental fatigue results for s 355 J2+N and comparison with the IIW recommendation.

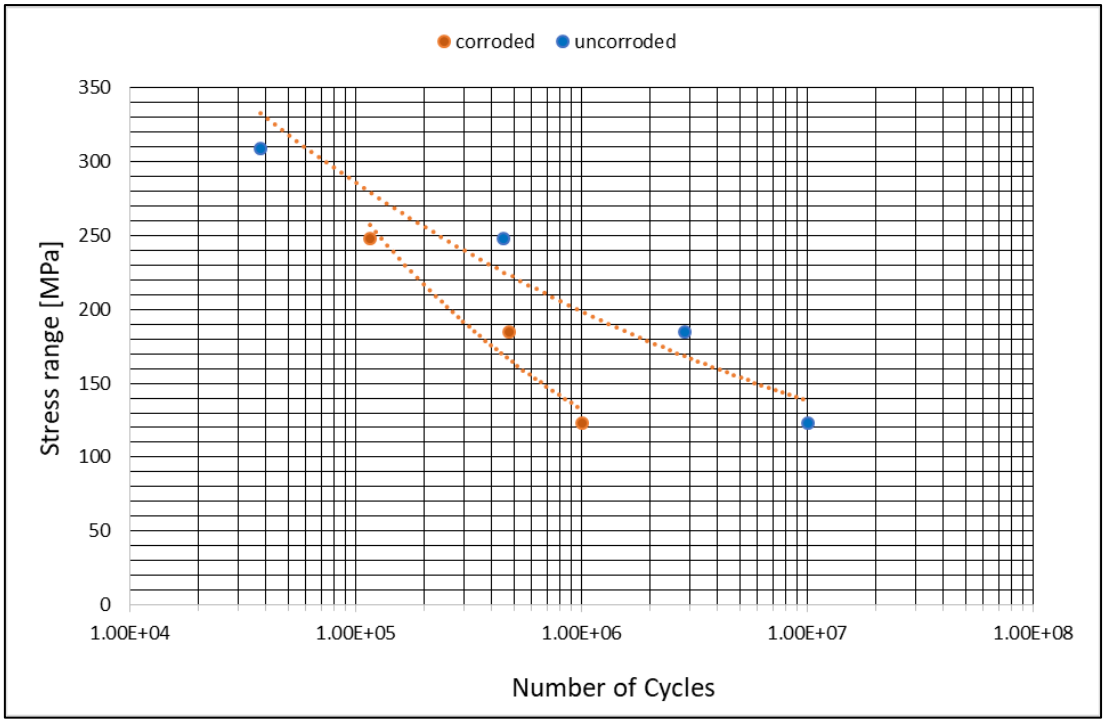

Figure 49: Experimental fatigue results for 316 Ti butt welds (uncorroded and corroded samples).

FATIGUE CRACK INITIATION

The SEM observations provide a microscopic view of fatigue crack initiation and propagation mechanisms, complementing the broader mechanical performance data. For HY 100 (Figures 50, 51), the corroded samples reveal fatigue crack initiation predominantly on the surface likely at corrosion pits or roughened areas caused by environmental degradation. These pits act as stress concentrators, reducing the material's resistance to cyclic loading. This observation aligns with the significant reduction in fatigue life reported for HY 100 in corroded conditions.

For S355 (Figures 52, 53, 54), the uncorroded samples demonstrate fatigue crack initiation at the surface as well, but without the presence of surface irregularities typical of corrosion. The progression of cracks shows distinct striations, indicative of stable cyclic crack growth. In corroded samples (Figures 55, 56), however, the SEM images reveal a similar initiation mechanism to that observed in HY 100 corroded samples, with corrosion pits significantly influencing crack formation. The propagation paths in these samples may also show more irregular patterns due to interactions with corrosion-induced defects.

These SEM findings reinforce the earlier discussion of the materials' performance under corrosive environments. They underscore the critical role of surface conditions and

environmental exposure in influencing fatigue crack initiation and propagation, particularly for materials like HY 100 and S355, which show reduced resistance to corrosion-induced damage. The correlation between microscopic features (corrosion pits and striations) and macroscopic fatigue performance highlights the need for surface treatments or protective measures to enhance durability.

Integrating this microscopic evidence with the previously analyzed fatigue data provides a more comprehensive understanding of material behavior under combined mechanical and environmental stress. For instance, the SEM observations explain why 316 Ti, with its superior corrosion resistance, would likely show fewer surface defects and improved fatigue performance in similar conditions.

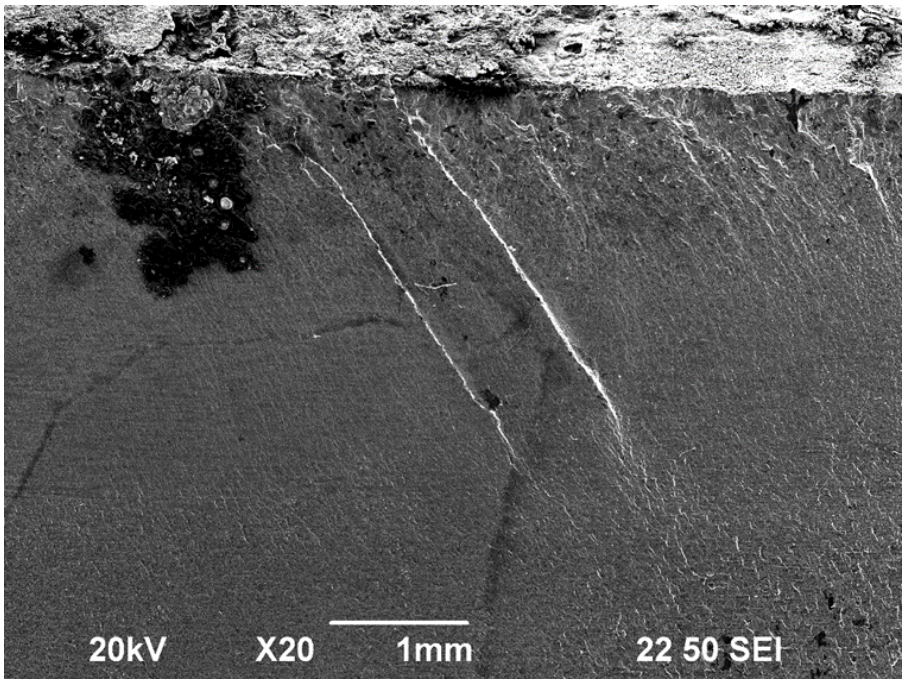

Figure 50: HY 100 corroded

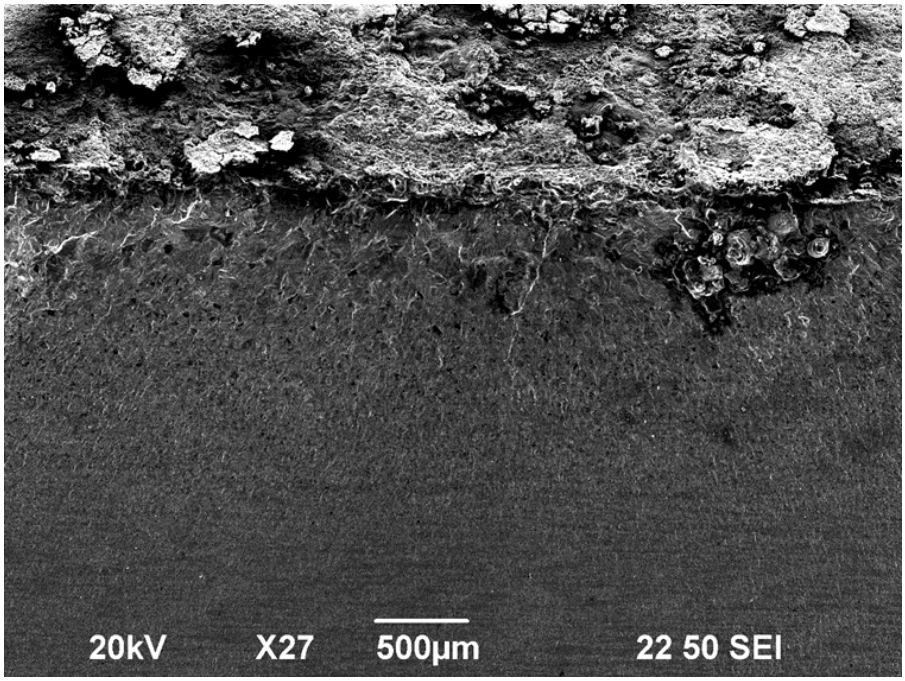

Figure 51: HY 100 corroded

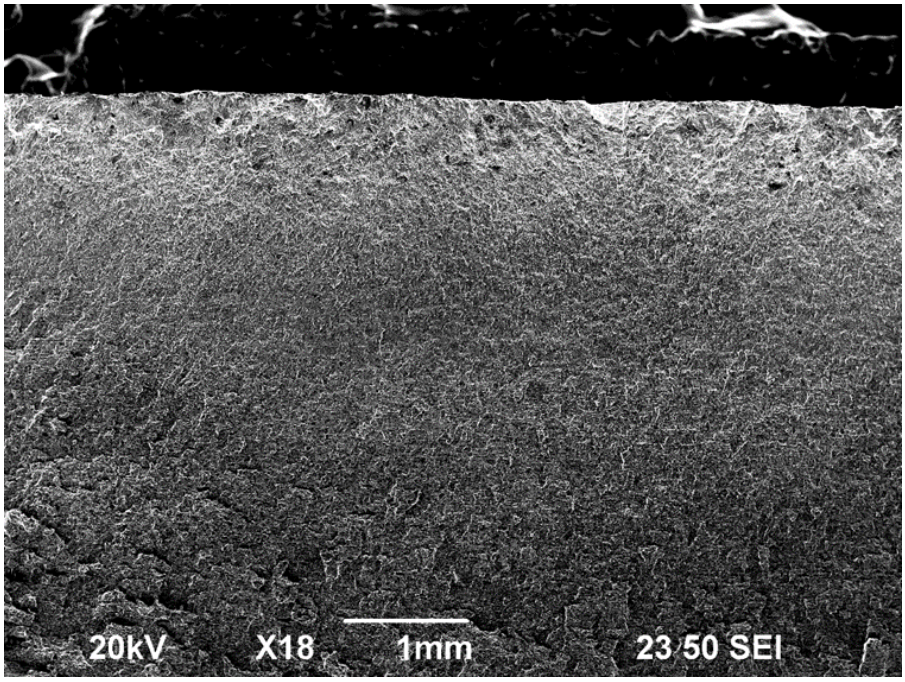

Figure 52: S355 uncorroded –Fatigue crack initiation (FACE).

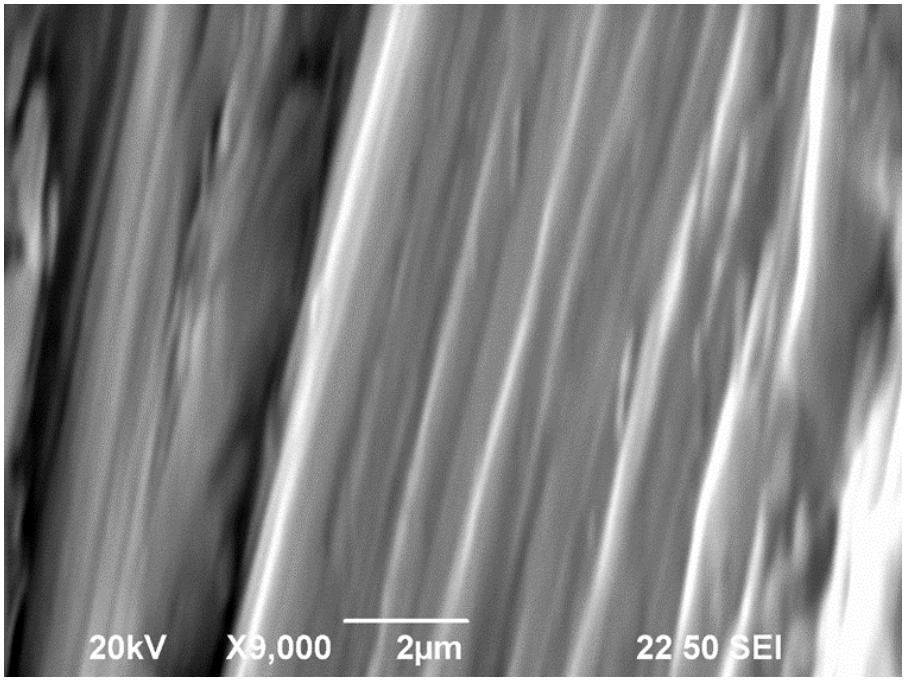

Figure 53: S355 uncorroded – fatigue crack propagation with striations.

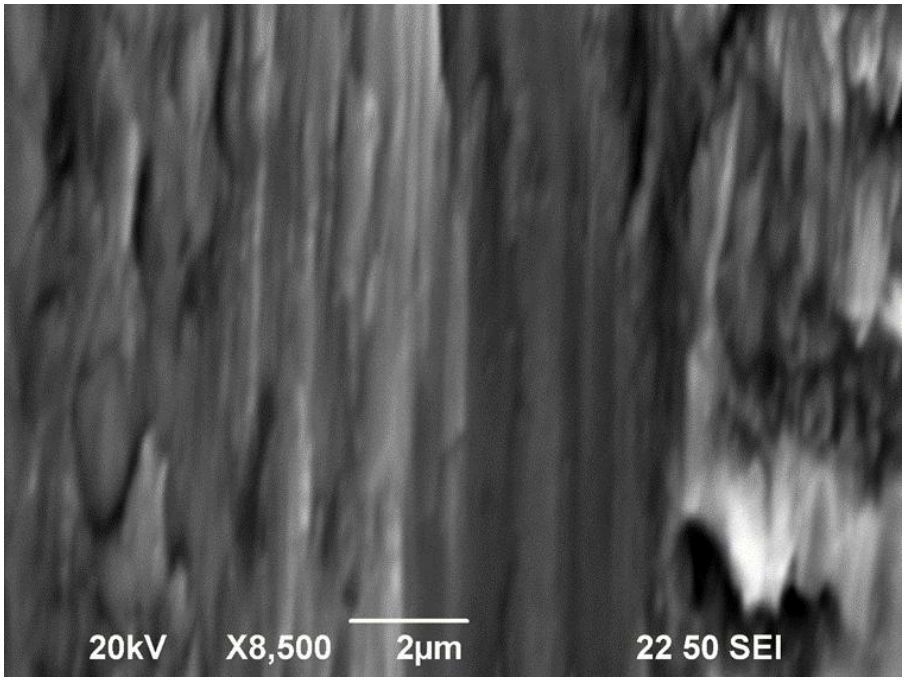

Figure 54: S355 uncorroded – fatigue crack propagation with striations.

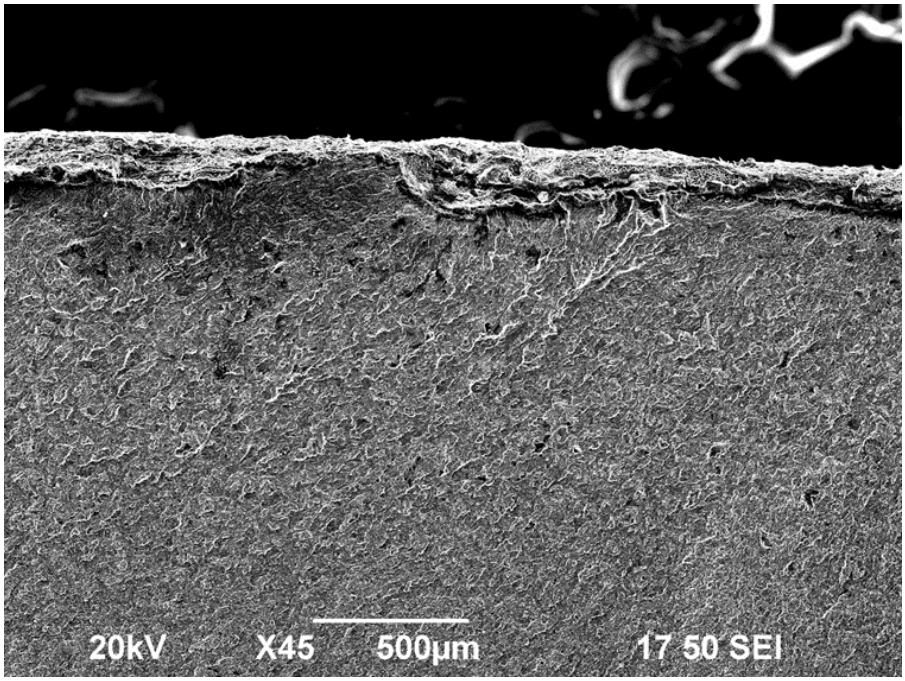

Figure 55: S355 corroded, Fatigue crack initiation (FACE)

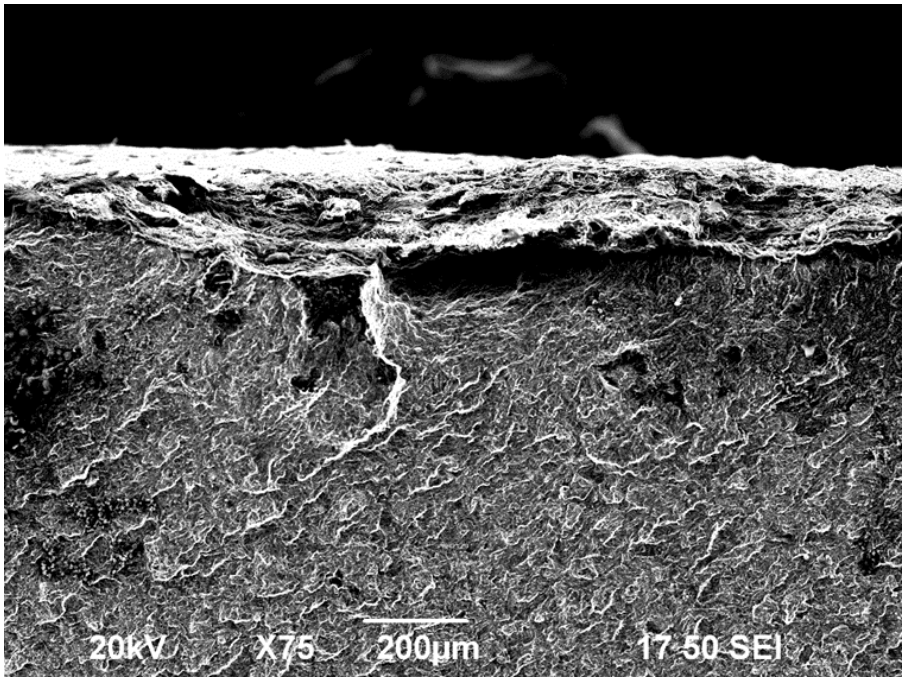

Figure 56: S355 corroded Fatigue crack initiation (FACE)

Chapter 5. Conclusion and Recommendations for Future Work

5.1 Conclusions

In the present work, the FCAW process was performed in HY100, 316Ti and S355J2+N steels with specific thickness (15mm and 10 mm). Taking into consideration the experimental results, interpretations, discussion and analysis the following outputs can be concluded:

i. After non-destructive evaluation, no defects were detected in each specimen because appropriate values of welding parameters were utilized.

ii. Welding current, welding voltage and welding speed are the most important welding parameters which influence the quality of the HY 100 steel welded joints, the 316Ti steel welded joints and the S355J2+N steel welded joints. The heat input in each welding layer must have low values such that qualitative welded joints are accomplished.

iii. Macroscopic examination did not illustrate any lack of sidewall fusion or another defect in the three welded joints under examination. The results of the welding experimental execution and of the metallographic examination can be the basis for the preparation of the final Welding Procedure Specification for each steel.

iv. The selection of the Salt Spray test was very advantageous for the determination of the corrosion resistance of the three welded specimens probably due to the fact that this method provides the relative results in an accelerated way. Additionally, the optical microscope and SEM analysis of each welded specimen provided very conclusive results about the corrosion morphology. Differences in the corrosion resistance were observed between the weld metal of the HY 100 and S355HJ2N welded specimens. The depth of the pitting corrosion is lower in the weld metal of the HY 100 welded steel specimen than the one in the weld metal of the S355J2 + N welded steel specimen. SEM/EDS analysis illustrated that despite the cleaning process performed after the completion of the Salt Spray test, a significant amount of Cl was trapped in the face of the weld metal of 316Ti welded steel specimen, while some amount of Cl was trapped in the face of the weld metal of HY 100 welded steel specimen. The 316Ti welded steel specimen illustrated the highest corrosion resistance, whereas the S355J2 + N welded steel specimen illustrated the lowest corrosion resistance. The corrosion resistance of the parent metal is affected by the chemical composition and the properties of the steels

under examination. The corrosion resistance of the weldments is affected by the selection and application of the relative welding process. The selection of the FCAW process (compared with other processes) for the welding execution illustrated that many metallurgical, mechanical and corrosion resistant advantages can be gained from the existence of the additional alloys which are included in the flux cored wire and, consequently, can improve the corrosion resistance of the welds.

v. The comparative analysis of HY 100, S 355 J2+N, and 316 Ti highlights significant differences in their fatigue performance, mechanical properties, and resistance to environmental factors. HY 100 exhibits moderate fatigue performance in uncorroded conditions but there is a significant reduction in fatigue life when exposed to corrosive environments. This reduction underscores its sensitivity to environmental degradation, such as saltspray exposure, which accelerates fatigue crack initiation and propagation. While its performance aligns moderately with IIW standards, its susceptibility to corrosion implies that additional safety factors may be required in design considerations for critical applications.

vi. S 355 J2+N, on the other hand, displays moderate-to-low fatigue limits, with a steeper reduction in fatigue life under corrosive conditions. This significant deterioration underlines the material's vulnerability to aggressive environments. While it shows good alignment with IIW standards in uncorroded states, its fatigue life diverges significantly when pre-corroded, suggesting that the standards may not adequately address environmental factors for this material. These findings highlight its limitations for high-cycle fatigue applications, particularly in offshore or marine environments where corrosion is prevalent.

vii. In contrast, 316 Ti outperforms the other two materials, exhibiting higher fatigue resistance in both uncorroded and corroded conditions. The reduction in fatigue life for 316 Ti due to corrosion is comparatively less pronounced demonstrating its reliability in environments where corrosion is a major concern. Although it has not been explicitly tested against IIW standards, its performance in fatigue and corrosion environments suggests it is well-suited for applications where these factors are critical, such as in the marine and chemical industries.

In conclusion, this research makes significant contributions to the understanding and application of the FCAW process for welding high-strength and corrosion-resistant steels, including HY100, 316Ti, and S355J2+N. The detailed analysis of welding parameters, such as

welding current, voltage, and speed, has demonstrated their critical role in ensuring high-quality welded joints, free from defects. The findings underline the importance of optimizing heat input to minimize defects and improve the integrity of the weldments. Additionally, the corrosion resistance study, particularly through the Salt Spray test, has provided valuable insights into the performance of welded joints in aggressive environments, highlighting the superior corrosion resistance of 316Ti compared to HY100 and S355J2+N. The comparative mechanical and fatigue analysis across these materials has clarified their behavior under both uncorroded and corrosive conditions, offering important data for material selection in real-world applications. The research also emphasizes the advantages of the FCAW process in enhancing the mechanical, metallurgical, and corrosion-resistant properties of welded joints through the use of flux cored wires. These findings contribute to the development of more reliable and durable welded structures, particularly in industries where environmental factors like corrosion and fatigue are prevalent. The knowledge gained from this study has the potential to inform welding procedures, material selection, and design considerations for critical applications in sectors such as offshore, marine, and chemical industries, thus making a valuable impact on the field of welding engineering and material science.

5.2 Future Scope of Work

It is worth mentioning that fatigue experiments under simultaneous exposure in corrosive environments shall be performed for the three materials under investigation.

References

Akita, M., Kakiouchi, T., Koama, A., Nakajima, M., Takase, T., Agata, Y., Takeo, Y., Imazato, S., Sugimoto, T., Uematsu, Y. (2018). Effect of weld metals on fatigue behavior of Nb-added ferritic stainless steel JFE429EX welds in laboratory air and in 3% NaCl solution, *Quarterly Journal of the Japan Welding Society*, 36 (4), 238-246

Alaskari, L., Liptáková, T., Fajnor, P., et al. (2014). Mechanical surface treatments effects on corrosion of AISI 316Ti stainless steel in chloride environments. Journal of Engineering Research, 2(1), 20.

Althouse, A. D., Turnquist, C. H., Bowditch, W. A., & Bowditch, K. E. (2020). **Modern Welding**. Goodheart-Willcox.

Ahmad,HW., Chaudry, UM., Tariq, MR., Shoukat, AA., Bae, DH. (2020). Assessment of fatigue and electrochemical corrosion characteristics of dissimilar materials weld between alloy 617 and 12 Cr steel, *Journal of Manufacturing Processes*,53, 275-282.

American Welding Society. (1987). **Welding Inspection Handbook (3rd ed.)**. Miami, FL: AWS.

American Welding Society. (1991). **Welding Handbook (Vol. 2, 8th ed.)**. Miami, FL: AWS.

American Welding Society. (1998). **Welding Handbook (Vol. 4, 4th ed.)**. Miami, FL: AWS.

American Welding Society. (1998). **Welding Handbook**. Miami, FL: AWS.

ASM International. (1994). *Metals Handbook*, Volume 1: Properties and Selection—Irons, Steels, and High-Performance Alloys. 10th Edition. ASM International.

Arivazhagan, B., Sundaresan, S., & Kamaraj, M. (2009). A study on the influence of shielding gas composition on toughness of flux-cored arc welds of modified 9Cr–1Mo (P91) steel. *Journal of Materials Processing Technology*, *209*(7), 5245–5253. https://doi.org/10.1016/j.jmatprotec.2009.02.006

Bailey, N., Coe, F. R., Gooch, T. G., Hart, P. H. M., Jenkins, N., & Pargeter, P. J. (1973). **Welding Steels Without Hydrogen Cracking**. Cambridge, England: Abington Publishing.

Bracarense, A. Q., Souza, R. L. de, & Liu, S. (2002). Welding current effect on diffusible hydrogen content in flux cored arc weld metal. *Journal of the Brazilian Society of Mechanical Sciences*, *24*(4), 1–1. https://doi.org/10.1590/S0100-73862002000400005

Brnić, J., Turkalj, G., Canadiya, M., & Lanc, D. (2011). AISI 316Ti (1.4571) steel—Mechanical, creep and fracture properties versus temperature. *Journal of Constructional Steel Research*, *67*(12), 1948–1952.

Choi, J., & Majumder, J. (2002). Numerical and experimental analysis for solidification and residual stress in the GMAW process for AISI 304 stainless steel. *Journal of Materials Science*, *37*(10), 2143–2158.

Davis, J.R. (1994) ASM Speciality Handbook Stainless Steels, ASM International.

Didonna, G., Bragotto, F., Rocha, R. (2020). PA-UT (Phased Array Ultrasonic Testing) qualification on fatigue sensitive high thickness cladded girth welds in compliance to DNV-QS-F101, *Rivista Italliana della Saldatura, 72 (3),* 321-331.

El Maya, M., Saintier, N., Palin-Luc, T., Devos, O., Brucelle, O. (2018). Modelling of corrosion fatigue crack initiation on martensitic stainless steel in high cycle fatigue regime, *Corrosion Science*, 133, 397-405

Fajnor, P., Liptáková, T., & Konstantová, V. (2010). Influence of AISI 316Ti stainless steel surface treatment on pitting corrosion in various solutions. *Materials Engineering*, *17*(3).

Flax, R. W., Keith, R. E., & Randall, M. D. (1971). **Welding the HY Steels**. American Society for Testing and Materials, New York, NY.

Gabler, U. (2000). **Submarine Design**. Bernand & Graefe Verlag, Bonn, Germany.

Gadallah, R., Fahmy, R., Khalifa, T., & Sadek, A. (2012). Influence of shielding gas composition on the properties of flux-cored arc welds of plain carbon steel. *International Journal of Engineering and Technology Innovation*, *2*(1), 1–12.

Gkatzogiannis, S., Weinert, J., Engelhardt, I., Knoedel, P., Ummenhofer, T. (2021). Corrosion Fatigue behavior of HFMI-threaded butt welds, *International Journal of Fatigue*, 145.

Gunaraj, V., & Murugan, N. (2002). Prediction of heat-affected zone characteristics in FCAW of steel structures. *Journal of Materials Processing Technology, 125*, 24–31.

Handbook of Radiographic Apparatus and Techniques. (1982). The International Institute of Welding. Abington Publishing, Cambridge, England.

International Institute of Welding. (1982). **Handbook of the Ultrasonic Examination of Welds**. Abington Publishing, Cambridge, England.

Jeffus, L. (2020). **Welding: Principles and Applications**. Cengage Learning.

Jie, Z., Berto, F., Susmel, L. (2020). Fatigue behaviour of pitted/cracked high-strength steel wires based on the SED approach, *International Journal of Fatigue,* 135

Jie, Z., Susmel, L. (2020). High-strength steel wires containing corrosion pits: stress analysis and critical distance based fatigue life estimation, *Fatigue & Fracture of Engineering Materials and Structures,* 43(8), 1611-1629

Knysh, VV., Solovei, S., Kir'yan, V.I., Bulash, V.N. (2018). Increasing the Corrosion Fatigue Resistance of Welded Joints by High-Frequency Mechanical Peening, *Strength of Materials*, 50 (3), 443-447

Lathabai, S., & Stout, R. D. (1985). Shielding gas and heat input effects on flux-cored weld metal properties. *Welding Journal Supplement*, 303–313.

Le Mehaute, B., & Hanes, D. M. (1990). **Ocean Engineering Science (Vol. 9)**. John Wiley & Sons, USA.

Lee, H.T., Shin, S.B. (2007). A Study of the Prediction of Shrinkage and Residual Stress for the HY-100 Weldment Considering the Phase Transformation. *Journal of KWJS,* Vol. 25, No. 1, 42-48.

Liu, Z., & Zhang, W. (2024). Comprehensive impact of machined surface integrity on stress corrosion cracking initiation in 316 austenitic stainless steel. *Journal of Materials Engineering and Performance, 33*(3), 369–380.

Mikkola, E., Marquis, G., Lehto, P., Remes, H., Hannine, H. (2016). Material characterization of high-frequency mechanical impact (HFMI) treated high strength steel, *Materials and Design*, 89, 205-214

Minnick, W. H. (2010). **Flux-Cored Arc Welding Handbook**. Goodheart-Willcox.

Morigaki, O., Matsumoto, T., & Takemoto, Y. (1976). Some improvements in self-shielded flux-cored electrodes for arc welding. *Welding Research Supplement*, 241–248.

Noga, P., Skrzekut, T., Wędrychowicz, M., Węglowski, S. T., & Wiewióra, M. (2020). The influence of various welding methods on the microstructure and mechanical properties of 316Ti steel. *Materials, 17*(7), 1681. https://doi.org/10.3390/ma17071681

Norrich, J. (2006). **Advanced Welding Processes (2nd ed.)**. Woodhead Publishing Limited, Cambridge, England.

Pang, W., Ahmed, N., & Dunne, D. (2011). Hardness and microstructural gradients in the heat-affected zone of welded low-carbon quenched and tempered steels. *Australasian Welding Journal, 56*(1), 34–48.

Parmar, R. S. (1992). **Welding Processes and Technology**. New Delhi: Khanna Publishers.

Pitrun, M. (2004) The effect of welding parameters on levels of diffusible hydrogen in weld metal deposited using gas shielded rutile flux cored wires. PhD Thesis, University of Wollongong, Australia.

Plum, R. M. (2015). **Fatigue crack detection on structural steel members by using ultrasound excited thermography**. KIT Scientific Publishing.

Reardon, A. C. (2011). **Metallurgy for the Non-Metallurgist (2nd ed.)**. Ohio: ASM International.

Rombado, G., Baker, D.A., Kan, WC., Craidy, P., Hudak, SJ. (2016). Fatigue life performance of titanium grade 29 welds in tapered stress joints, *Proceedings of the International Offshore and Polar Engineering Conference*, January, 2016, 606-611

Sadiq, I. O., Tairu, S. B., Garba, A. B., & Lawal, S. A. (2015). Effect of process parameters on the shielded metal arc welding of HY100 high strength low alloy steel. *International Journal of Advanced Research in Science, Engineering and Technology, 2*(3).

Shojai, S., Kabha, K., Woitzik, C., Braun, M., Ghafoori, E. (2025). Fatigue behaviour of 12-month corroded offshore steel joints under accelerated salt spray exposure: an experimental and numerical analysis. *Welding in the World*, 69, :2351–2369

Taban, E., Kaluk, E., Ojo, OO. (2016). Properties, weldability and corrosion behavior of supermartensitic stainless steels for on- and offshore applications, *Materials Testing*, 58 (6), 501-518

Tan, J., Wang, X., WU Xinqiang, Han En-Hou (2021). Corrosion Fatigue Behavior of 316LN Stainless Steel Hollow Specimen in High-Temperature Pressurized Water, *Jinshu Xuebao/Acta Metallurgica Sinica*, 57 (3), 309-316.

Wang, X., Yu, H., Li, X., Chen, S. (2016). Fatigue test analysis of ultra-high strength spot welded structure, *Transactions of the China Welding Institute*, 37 (2), 99-102 and 110

Weman, K. (2003). **Welding Processes Handbook (1st ed.)**. Cambridge, England: Woodhead Publishing Limited.

Yu, X., Yao, G., Gu, L., Fan, W. (2020). Numerical and Experimental Study on the Steel Strands under the Coupling Effect of a Salt Spray Environment and Cyclic Loads, *Materials*, 13 (3), 736

Zeng, D., Li, H., Tian, G., Liu, f., Lid, B., Yue, S., Ouyang, Z., Shi, T. (2018). Fatigue behavior of high-strength steel S135 under coupling multi-factor in complex environments, *Materials Science and Engineering: A*, 724, 385-402

Zheng, K., Zhang, Y., Heng, J., Wang, Y. (2020). High strength weathering steel and its application and prospect in bridge engineering, *Journal of Harbin Institute of Technology*, 52 (3), 1-10

Zielińska, S., Valensi, F., Pellerin, N., & Briand, F. (2009). Microstructural analysis of the anode in gas metal arc welding (GMAW). *Journal of Materials Processing Technology*, *209*(8), 3581–3591.